Modeling Hydrogen Diffusion in a Tribological Scenario: A Failure Analysis of a Thrust Bearing

Iyas Khader[1,2], Dominik Kürten[2], Rahul Raga[2], Nicholas Winzer[2], Andreas Kailer[2]

[1] Department of Industrial Engineering, German-Jordanian University, P.O. Box 35247, 11180 Amman, Jordan

[2] Fraunhofer Institute for Mechanics of Materials IWM, Wöhlerstr. 11, 79108 Freiburg, Germany

Abstract

A coupled diffusion-mechanical finite element simulation model was developed to study the diffusion of hydrogen in a cylindrical roller thrust bearing (CRTB). The simulations enabled obtaining qualitative information pertaining to stress-assisted diffusion in tribological loading and under the influence of residual stresses. The mechanical behavior of bearing steel was obtained from experiments and supported by literature. In parallel, rolling-contact fatigue (RCF) tests on CRTBs lubricated with a fully additivated transmission oil were conducted for 25 h and 50 h to investigate their premature failure modes.

Post-RCF rheological analysis indicated decrease of the lubricant viscosity due to degradation. Carrier gas hot extraction analysis indicated a significant increase in hydrogen content in the bearings tested for 50 h. Whereas, serial cross-sectional analysis revealed the formation of subsurface White Etching Crack (WEC) networks associated with White Etching Areas (WEA); the cracks breached the surface on multiple positions causing flaking and eventual failure. On the other hand, no signs of damage were observed in the bearings tested for 25 h.

The simulations revealed insignificant hydrogen accumulation due to stress-assisted diffusion in comparison to concentration gradient driven diffusion; hydrogen trapping was pronounced in zones undergoing plastic deformation due to the formation of deformation induced trapping sites. However, residual stresses had an evident influence on the subsurface accumulation of hydrogen. A comparison between the zones of elevated hydrogen concentration due to residual stresses and RCF induced subsurface damage yielded a good correlation.

Keywords: Hydrogen diffusion, roller bearing, lubricant degradation, white etching cracks, white etching areas, residual stress

1. Introduction

Steel rolling elements in bearings are known to undergo premature failure due to brittle flaking or what is also known as white structure flaking as observed in lab tests and actual field application [1, 2, 3, 4, 5]. This failure mode is associated with the formation of white etching areas (WEA). Hydrogen-assisted rolling contact fatigue (HARCF) is often proposed as the culprit or accelerator of material degradation leading to this specific failure mode. In lubricated tribological contact, as in the case of bearings, a body of literature suggests that the hydrogen is generated due to lubricant degradation through tribochemical reactions [6, 7, 8, 9, 10]. In a series of vacuum-tribometery investigations [9, 10], it was shown that hydrogen evolution due to lubricant decomposition under tribological loading is dependent on the chemical composition of the lubricant. In a recent study [11] it was shown that bearings lubricated with a non-hydrocarbon-based lubricant, which does not release hydrogen due to tribochemical decomposition, did not show any signs of premature damage (white etching cracks (WEC), WEA or brittle flaking) in rolling contact fatigue (RCF) tests but rather signs of delayed fatigue damage in the form of dark etching areas. The hydrogen-induced embrittlement mechanism in steel is not yet well understood and is a current topic of research and hence, understanding the factors affecting diffusion and subsurface accumulation of hydrogen in bearing steel is crucial to the development of measures to mitigate or completely eliminate its detrimental effect.

Early attempts of numerical modeling of stress-assisted hydrogen diffusion in metals [12, 13, 14, 15] have shown that hydrogen flux is generated towards regions of tensile hydrostatic stress such as in the vicinity of crack tips. Modeling hydrogen diffusion in tribological contact forms a challenging task due to the hydrogen repelling nature of the predominantly compressive stresses engendered within the contact zone. Winzer and Khader [16] modeled hydrogen diffusion and trapping in a twin-disk configuration using a weakly coupled finite element (FE) based model. On the other hand, Kadin [17] conducted an FE based study on the effect of Hertzian contact stresses on hydrogen diffusion. Both works concluded that

stress-assisted diffusion played a minor role in the accumulation of hydrogen. Kruhöffer and Loos [18] attempted to correlate the formation of white etching cracks (WEC) with asperity frictional energy accumulation in a cylindrical roller thrust bearing (CRTB) by applying a micromechanical contact model. A general review on modeling research activities addressing hydrogen related failures in metals was compiled by Díaz et al. [19]. On the other hand, a more recent approach of fully coupling the diffusion process with the mechanical response of the material was accomplished for hydrogen by [20, 21, 22, 23, 24, 25] and for oxygen by [26]. The coupling was possible by relying on the analogy between mass and heat transfer as described by Prussin [27].

Heat treatment and machining operations conducted on bearing components result in residual stresses dependent on the processes itself and the composition of the steel. The effect of exponentially-decaying residual stresses on hydrogen diffusion in rolling-contact did not show any significant influence on the maximum hydrogen concentration [16]. Several researchers have measured residual stress profiles in bearing components [28, 29, 30, 31]. Recently, Gould et al. [32] measured residual stress profiles in through-hardened AISI 52100 steel samples that were tested in a micro pitting rig to study the effect of microstructure on the formation of WEC. Generally, highly compressive residual stresses appear in the surface layer and weaker tensile stresses appear below it in the depth. In the study conducted by Voskamp et al. [28], it was shown that surface compressive residual stresses are somehow reduced by over-rolling, whereas, subsurface tensile stresses are retained at small depths whereas, at greater depths tensile stresses change to compressive after a certain number of stress cycles, depending on the extent of the subsurface plastic deformation.

In this work, the diffusion of hydrogen in a CRTB was investigated. A three-dimensional simulation of the bearing was modeled in the finite element software package Abaqus 2018. The mechanical model was implemented through the user subroutine UMAT, which enables coupling the mechanical and thermophysical behavior of the material through a further implementation of the user subroutine

UMATHT. Hence, by relying on the analogy between mass and heat transfer, UMATHT was modified to model mass diffusion into the material. The advantage of this construct lies with the possibility of running a simultaneous fully coupled diffusion-mechanical simulation, which enables updating the diffusion of a certain species according to the stress-strain state and simultaneously, adapting the mechanical response of the material based on the concentration of the diffusing species. A comprehensive treatment of this topic is found elsewhere [21, 22].

The aim of this work is to model stress-assisted hydrogen diffusion in a CRTB through a fully coupled diffusion-mechanical finite element simulation. The research will focus on the effect of stresses on the diffusion and accumulation of hydrogen. The numerical simulations were conducted by relying on experimentally-measured mechanical behavior in actual bearing steel. The numerical results were correlated with failure modes observed in bearings tested on a custom built RCF test rig.

2. Hydrogen diffusion and trapping model

Considering the theory of hydrogen diffusion by moving through normal interstitial lattice sites (NILS), the NILS concentration is given by

$$C_L = \beta \theta_L N_L$$

1

where C_L is the hydrogen concentration per lattice volume (atom/mm^3), β is the number of interstitial sites (NILS) per solvent atom, θ_L is the fraction of lattice sites occupied by hydrogen atoms, $0 \leq \theta_L \leq 1$, and N_L is the number of solvent lattice atoms per unit lattice volume (atoms/mm^3), given by

$$N_L = \frac{\rho N_A}{A_r}$$

2

where ρ is the density, N_A is Avogadro's number (6.022×10^{23} atoms/mole) and A_R is the molar mass of the solvent atom. The hydrogen concentration at traps is given by

$$C_T = \alpha \theta_T N_T$$

3

where α denotes the number of atom sites per trap, θ_T is the fraction of trapping sites occupied by hydrogen atoms, $0 \le \theta_T \le 1$, and N_T is the number of atomic trapping sites along the total dislocation line length per unit volume, which is an implicit function of the plastic strain. A range of experimentally-determined values for N_T in iron was estimated by Kumnick and Johnson [33]. The trapping site density can be expressed as function of the dislocation density as follows

$$N_T = \frac{N_b \vartheta}{b} \qquad\qquad 4$$

where ϑ is the dislocation density (mm^{-2}), N_b is the number of trap sites per Burgers vector b, which for BCC and FCC lattices can be given in terms of the lattice parameter a by

$$\|b\| = \frac{a}{2}\sqrt{h^2 + k^2 + l^2} \qquad\qquad 5$$

where h, k, and l are its components. In most metallic materials, the magnitude of the Burgers vector is a good approximation of the interatomic spacing of the material. Due to insufficient data, N_b will be maintained at unity throughout this study. The change in dislocation density as function of strain may be approximated by the formula proposed by Hahn et al. [34]

$$\vartheta = \vartheta_0 + \gamma \left(\epsilon^{pl}\right)^{\phi} \qquad\qquad 6$$

where ϵ^{pl} is the equivalent plastic strain $\epsilon^{pl} = \int_0^t \sqrt{\frac{2}{3}\dot{\epsilon}^{pl}:\dot{\epsilon}^{pl}} dt$ given in terms of the equivalent plastic strain rate $\dot{\epsilon}^{pl}$. ϑ_0 is the dislocation density for annealed material, $\vartheta_0 = 10^4$ mm^{-2}, and γ and φ are material specific constants set, in accordance with the range of values given by Yoshida et al. [35], to $\gamma = 1.0 \times 10^8$ mm^{-2} and $\varphi = 1.0$.

In what follows, molar quantities will be expressed by a bar over the symbol.

For the treatment of hydrogen diffusion into a solid, the diffusion problem is defined from the requirement of mass conservation for the diffusing phase as follows:

$$\frac{\partial}{\partial t}\int_V \bar{C}\,dV + \int_{\partial V} \mathbf{n}\cdot\bar{\mathbf{F}}\,dS = 0 \qquad\qquad 7$$

where V is any volume whose surface is S, $\mathbf{n}$ is the outward normal to S and the total concentration of hydrogen is expressed in terms of the lattice and trap concentrations [36] as follows:

$$\bar{C} = \bar{C}_L + \bar{C}_T \qquad\qquad 8$$

The flux $\bar{\mathbf{F}}$ in Eq. 7 can be expressed by

$$\bar{\mathbf{F}} = -\frac{D_L \bar{C}_L}{RT}\nabla\mu \qquad\qquad 9$$

where D_L is the lattice diffusivity, R is the universal gas constant, T is the absolute temperature in kelvins and $\nabla\mu$ is the spatial gradient of the chemical potential, which is considered the driving force of diffusion.

The lattice diffusivity D_L is defined in terms of the diffusion pre-exponent D_o, the activation energy for diffusion E_D, the ideal gas constant R, and the absolute temperature in kelvins T as follows

$$D_L = D_o e^{\left(-\frac{E_D}{RT}\right)} \qquad\qquad 10$$

The lattice diffusivity D_L and the effective diffusion coefficient D_{eff} can be described with the following equation [37]

$$D_{eff} = D_L \frac{C_L}{C_L + C_T(1 - \theta_T)} \qquad\qquad 11$$

and the generalized chemical potential of this system is defined by

$$\mu = \mu_0 + RT\ln\bar{C}_L - \mu_\sigma \qquad\qquad 12$$

where μ_0 is a reference value and μ_σ is the stress dependent part of the chemical potential. Assuming that NILS hydrogen causes only dilational distortion to the lattice, hence, μ_σ can be written as

$$\mu_\sigma = \sigma_h \bar{V}_H \qquad\qquad 13$$

where σ_h is the hydrostatic stress ($\sigma_h = -\frac{1}{3}trace(\boldsymbol{\sigma}) = -\frac{1}{3}\sum_{k=1}^{3}\sigma_{kk}$) and $\bar{V}_H$ is the partial molar volume of hydrogen dissolved in the host material [38].

Using the form described by Sofronis and McMeeking [12] results in a constitutive expression of the flux equation

$$\bar{\mathbf{F}} = \frac{D_L \bar{V}_H \bar{C}_L}{RT} \nabla \sigma_h - D_L \nabla \bar{C}_L \qquad\qquad 14$$

where $\nabla \sigma_h$ and $\nabla \bar{C}_L$ are the spatial gradients of the hydrostatic pressure and concentration, respectively.

Substituting Eq. 14 into Eq. 7 yields the form

$$\frac{\partial}{\partial t} \int_V \bar{C} dV + \int_{\partial V} \mathbf{n} \cdot \left(\frac{D_L \bar{V}_H \bar{C}_L}{RT} \nabla \sigma_h - D_L \nabla \bar{C}_L \right) dS = 0 \qquad\qquad 15$$

and by applying the divergence theorem

$$\frac{\partial \bar{C}}{\partial t} + \nabla \left(\frac{D_L \bar{V}_H \bar{C}_L}{RT} \nabla \sigma_h \right) - \nabla (D_L \nabla \bar{C}_L) = 0 \qquad\qquad 16$$

From Eq. 8

$$\frac{\partial \bar{C}_L}{\partial t} + \frac{\partial \bar{C}_T}{\partial t} + \nabla \left(\frac{D_L \bar{V}_H \bar{C}_L}{RT} \nabla \sigma_h \right) - \nabla (D_L \nabla \bar{C}_L) = 0 \qquad\qquad 17$$

Applying the chain rule, the partial derivative of hydrogen concentration in traps with respect to time is given by

$$\frac{\partial \bar{C}_T}{\partial t} = \frac{\partial \bar{C}_T}{\partial \bar{C}_L} \frac{\partial \bar{C}_L}{\partial t} + \frac{\partial \bar{C}_T}{\partial \bar{N}_T} \frac{\partial \bar{N}_T}{\partial \epsilon^{pl}} \frac{\partial \epsilon^{pl}}{\partial t} \qquad\qquad 18$$

from which Eq. 17 becomes

$$\frac{\partial \bar{C}_L}{\partial t} + \frac{\partial \bar{C}_T}{\partial \bar{C}_L} \frac{\partial \bar{C}_L}{\partial t} + \frac{\partial \bar{C}_T}{\partial \bar{N}_T} \frac{\partial \bar{N}_T}{\partial \epsilon^{pl}} \frac{\partial \epsilon^{pl}}{\partial t} + \nabla \left(\frac{D_L \bar{V}_H \bar{C}_L}{RT} \nabla \sigma_h \right)$$
$$- \nabla (D_L \nabla \bar{C}_L) = 0 \qquad\qquad 19$$

and by re-writing the spatial gradients in terms of the coordinate system **x**, Eq. 19 becomes

$$\frac{\partial \bar{C}_L}{\partial t} + \frac{\partial \bar{C}_T}{\partial \bar{C}_L}\frac{\partial \bar{C}_L}{\partial t} + \frac{\partial \bar{C}_T}{\partial \bar{N}_T}\frac{\partial \bar{N}_T}{\partial \epsilon^{pl}}\frac{\partial \epsilon^{pl}}{\partial t} + \frac{\partial}{\partial \mathbf{x}}\left(\frac{D_L \bar{V}_H \bar{C}_L}{RT}\frac{\partial \sigma_h}{\partial \mathbf{x}}\right)$$
$$- \frac{\partial}{\partial \mathbf{x}}\left(D_L \frac{\partial \bar{C}_L}{\partial \mathbf{x}}\right) = 0 \qquad\qquad 20$$

assuming time invariant number of lattice sites and constant temperature, the partial derivative of Eq. 18 becomes

$$\frac{\partial \bar{C}_T}{\partial t} = \frac{\bar{C}_T(1 - \theta_T)}{\bar{C}_L}\frac{\partial \bar{C}_L}{\partial t} + \alpha\theta_T \frac{d\bar{N}_T}{d\epsilon^{pl}}\frac{\partial \epsilon^{pl}}{\partial t} \qquad\qquad 21$$

substituting into Eq. 20 yields the form introduced by Krom et al. [15]

$$\frac{\partial \bar{C}_L}{\partial t} + \frac{\bar{C}_T(1 - \theta_T)}{\bar{C}_L}\frac{\partial \bar{C}_L}{\partial t} + \alpha\theta_T \frac{d\bar{N}_T}{d\epsilon^{pl}}\frac{\partial \epsilon^{pl}}{\partial t} + \frac{\partial}{\partial \mathbf{x}}\left(\frac{D_L \bar{V}_H \bar{C}_L}{RT}\frac{\partial \sigma_h}{\partial \mathbf{x}}\right)$$
$$- \frac{\partial}{\partial \mathbf{x}}\left(D_L \frac{\partial \bar{C}_L}{\partial \mathbf{x}}\right) = 0 \qquad\qquad 22$$

In this work, Oriani's theory [37], which assumes local thermodynamic equilibrium between mobile and trapped hydrogen was adopted. Other models, e.g., Toribio and Kharin [39], do not rely on the assumption of local equilibrium of hydrogen between dissimilar sites. Following the approach by Svoboda and Fischer [40], and by defining an equilibrium constant (K_{eq}), the ratio between θ_T and θ_L may be expressed as

$$\frac{\theta_T}{\theta_L} = \frac{1}{K_{eq} + \theta_L(1 - K_{eq})}; \quad K_{eq}\frac{\theta_T}{1 - \theta_T} = \frac{\theta_L}{1 - \theta_L} \qquad\qquad 23$$

where K_{eq} is defined as the ratio of the rate of hydrogen atoms jumping from traps to lattice sites, λ, to the rate of hydrogen atoms jumping from lattice to trap sites, κ, and is given by

$$K_{eq} = \frac{\kappa}{\lambda} = e^{\left(-\frac{\Delta E_B}{RT}\right)} \qquad\qquad 24$$

where ΔE_B is the trap binding energy (a negative quantity), R is the ideal gas constant and T is the absolute temperature in kelvins.

For low NILS, i.e., $\theta_L \ll 1$, the fraction of trapping sites occupied by hydrogen atoms is given by

$$\theta_T = \frac{K_{eq}\theta_L}{(1 + K_{eq}\theta_L)} \qquad\qquad 25$$

3. Finite Element Modelling

The bearing was modelled using a coupled diffusion-mechanical three-dimensional finite element simulation in Abaqus. By relying on the analogy between mass and heat transfer the coupling between the diffusion processes and the mechanical behavior was accomplished by running a coupled temperature-displacement analysis in Abaqus/Standard. Having a fully-coupled model is indispensable in order to simulate the diffusion processes under cyclic loading.

The model was comprised of one roller in contact with the surfaces of the upper and lower rings. The geometry of the roller was obtained by measuring and analyzing its surface contour using optical microscopy, laser profilometry and stylus profilometry. Both ring raceways were modelled as flat surfaces. The rolling elements of the CRTB at hand are not cylindrical but rather slightly crowned and with filleted edges. The function of the barreling and edge fillets is: (i) to eliminate stress raiser at sharp edges and (ii) to ensure proper contact during operation since a pure line contact may give rise to unstable rolling behavior. This peculiar design results in an elliptical contact zone between the roller and raceways (cf. Kruhöffer and Loos [18]). The dimensions of the bearing and a section of the FE mesh are shown in Figure 1.

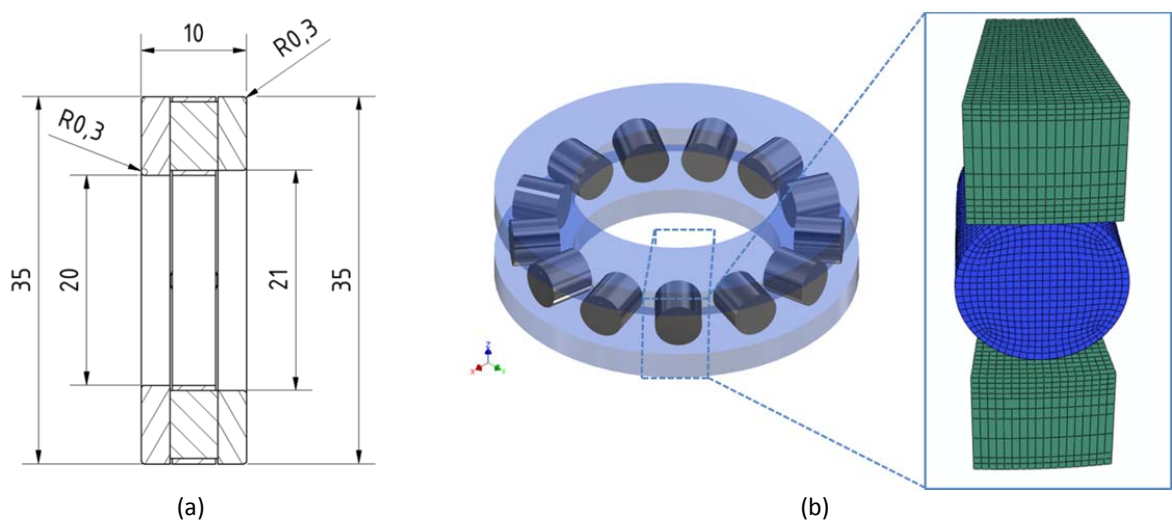(a)   (b)

Figure 1. (a) Dimensions of the bearing FAG 81104-TV in mm [41]; (b) three-dimensional finite element mesh section of the bearing without the cage

In order to resolve contact stresses with an acceptable accuracy while maintaining a reasonable size, second order elements were used in the roller. This was also a necessary step to account for stress-assisted diffusion, the reason for which will be discussed in Section 3.3. The average element size adjacent to the contact surface was 100×90×25 [µm]. Twenty-node second-order reduced integration hexahedral elements with displacement and temperature degrees of freedom (C3D20RT) were used to discretize the geometry of the roller. Eight-node first-order reduced integration hexahedral elements with displacement and temperature degrees of freedom (C3D8RT) were used to discretize the geometry of both upper and lower rings. A predefined normal force of 800 N was applied to one of the rings to initiate contact and exert the working load. At such load, the minor axis of the contact ellipse is about 200 µm spanning three elements. By using second-order elements with three nodes along each element edge length, the contact patch will be modeled by five to seven nodes, which is adequate to simulation the system with acceptable accuracy.

Despite being computationally intensive, an accurate depiction of the triaxial stress state, required for the diffusion analysis, can only be obtained from a three-dimensional model. This presented a challenge in modelling the rigid body motion of the roller (i.e., rolling contact), which becomes unrealistic to solve in a Lagrangian perspective and not possible in an Eulerian-Lagrangian analysis (as described in a previous study [42]), due to the fact that the latter does not couple the mechanical and thermal (in our case diffusion) solutions. This conflict was resolved by neglecting friction (the measured coefficient of friction (COF) was $\mu=0.005$, refer to Section 5.2) between the roller and the raceways and by modeling a roller rotating five times about its own axis, and hence, it was sufficient to model a small segment of the rings. To verify the stress distribution, the model was then compared with a full bearing model (described in Section 3.4). The effect of friction on surface stresses was also investigated by Zwirlein et al. [43] and was found to be negligible for low COF values (up to $\mu=0.05$). This approach enabled the simulation of the system with actual rigid body rotations to reproduce the effect of a shakedown phase

occurring after the first few rotations, after which it is assumed that a steady-state distribution of defects and hence, dislocation density, is attained within the material.

3.1. Material model

The mechanical model of steel 100Cr6 (ASTM 52100) was implemented through the user subroutine UMAT [44]. The material behavior was assumed to be isothermal, linear elastic with linear kinematic plasticity hardening. Linear kinematic plasticity has been adopted for 100Cr6 bearing steel by several researchers [45, 46] with hardening curve following the equation

$$\sigma_f = \sigma_0 + H\epsilon^{pl}$$

26

where σ_f is the flow stress, σ_0 is the material's (initial) yield strength, H is the hardening modulus and ϵ^{pl} is the true plastic strain. The mechanical properties of 100Cr6 were measured in a tensile test (refer to Section 4.1) and then compared to published values found in [47, 34]. The values used in the simulations are summarized in Table 1.

The simulations were carried out with two sets of mechanical properties that differ in terms of the initial yield strength (σ_0). This enabled studying the effect of plasticity on trapped hydrogen. To simplify the model, the hardening behavior was identical for both values of the initial yield strength. Additionally, it was assumed that hydrogen concentration has no influence on the mechanical behavior.

Table 1. Mechanical material properties of 100Cr6

Property	Unit	Value	Reference
Elastic modulus	GPa	200.2	Measured; refer to Section 5.1
Poisson's ratio	-	0.3	[47]
Initial yield strength (σ_0)	MPa	1195.1	Measured; refer to Section 5.1
Reduced Initial yield strength (σ_{0-red})	MPa	1000.0	[34]
Hardening modulus (H)	GPa	185.50	Measured; refer to Section 5.1

The diffusion model was implemented through UMATHT [44], which originally allows defining a thermal constitutive behavior of the material. UMATHT was modified to take advantage of the analogy between mass and heat transfer in order to model hydrogen diffusion in the bearing steel. The constants and material data required for the modeling of diffusion are listed in Table 2.

3.2. Diffusion boundary conditions

Due to the uncertainty regarding the mechanism for hydrogen generation, adsorption and absorption two sets of hypothetical boundary conditions were investigated. In all simulations, the release of hydrogen from steel into the atmosphere was not taken into consideration and an initial hydrogen concentration of 1.5 ppm (2.27×10^{-10} mol/mm^3) in the roller steel was assumed. The value was adopted based on the average hydrogen concentration determined through a series of measurements, refer to Section 5. The simulation time was set to 1.8×10^5 s, which corresponds to 50 h.

3.2.1. Hydrogen diffusion in bearing contact

The most straightforward method to trigger diffusion is by maintaining a constant concentration of hydrogen on the outer surface of the roller, Figure 2a. This however, entails fixing a predefined concentration at surface nodes independent of the contact state and its corresponding stresses, and

thus, defeats the purpose of the simulation model. This restriction was overcome by maintaining a predefined constant hydrogen concentration (assumed to be ten times that of the initial concentration, i.e., 2.27×10^{-9} mol/mm^3) on the counter surface (raceway surface), Figure 2b. Hence, hydrogen was assumed to be released and ad/absorbed during the contact cycle and from within the confinement of the contact zone upon loading only. The diffusion process was triggered when the two contacting surfaces reached a predefined clearance of 10 µm, which was estimated based on the roller curvature. It should be noted that hydrogen could certainly be present in the form of environmental water, from the polymeric cage or from the steel components; nonetheless, in this work, it was assumed that the degradation of the lubricant is the major contributor of hydrogen in the system.

3.2.2. Hydrogen diffusion in the presence of residual stress fields

A second set of boundary conditions was applied to study the effect of residual stress distribution on stress-assisted diffusion. Residual stress profiles (profile shape not stress magnitude) obtained by Voskamp et al. [28], and later confirmed in an independent study by Dommarco et al. [29], were adopted and implemented here as initial conditions prior to diffusion for three distinct cases:

I. Without any residual stresses in the material (stress profile referred to as *w/o residual stress*)

II. Compression field at the surface followed by a field of tensile stress in the depth to simulate through-hardened material in its virgin state (referred to as *C-T*)

III. Compression field at the surface (lower in magnitude than in the case C-T) followed by a tensile stress field below it, followed by another compressive stress field at greater depths (i.e., a tensile stress field trapped in between two compressive stress fields) to simulate a through-hardened roller that has undergone accumulation of subsurface plastic deformation (referred to as *C-T-C*)

Table 2. Material data required for the diffusion model

Property	Unit	Value	Reference(s)
D_o	mm^2/s	7.5×10^{-3}	[21]
E_D	mJ/mol	20.0×10^6	
β	-	6	
ρ	t/mm^3	7.874×10^{-9}	
A_R	u	55.845	
α	sites/trap	1.0	
$a_{\text{Fe}-\text{FCC}}$	mm	0.3571×10^6	
ϑ_0	mm^{-2}	1.0×10^4	[35]
γ	mm^{-2}	1.0×10^8	[48]
φ	-	1.0	
ΔE_B	mJ/mol	-60.0×10^6	[33]
R	mJ/mol.K	8.314×10^3	
$\bar{V}_H$	mm^3/mol	2.3×10^3	[38]

(a)   (b)
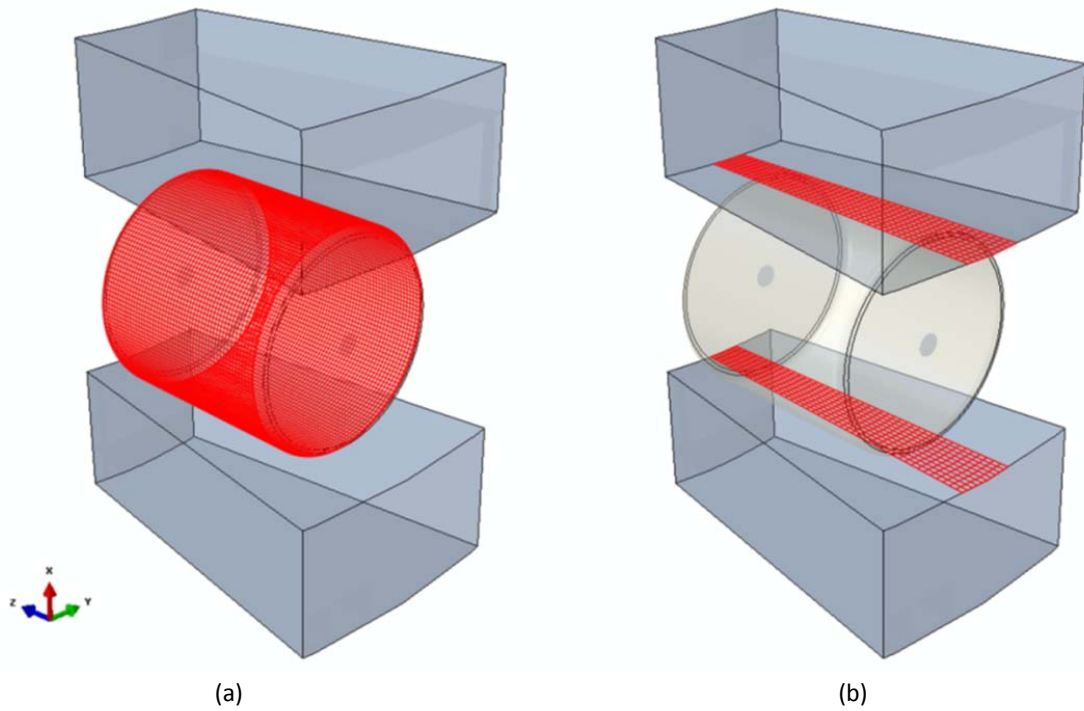
Figure 2. Hydrogen concentration maintained constant at (a) the roller surface, (b) the counter surface

These simulations were performed by assuming a stationary roller, whereas hydrogen was assumed to diffuse by surface flux from all surface nodes equally. A hypothetical value of 5×10^{-8} ppm·mm^3/s was set for the hydrogen influx.

3.3. Computation of pressure gradients

As shown in Eq.14, the constitutive equation of the flux requires the extraction of the hydrostatic pressure gradient $\nabla\sigma_h$ for each element. This is not readily available in Abaqus and hence, should be accomplished through a customized subroutine. As pointed out in the literature, there are mainly two methods followed to compute the pressure gradient. The first method involves calculation of pressure gradients using the subroutine USDFLD in combination with the utility subroutine GETVRM to obtain pressure gradients for each increment. However, since Abaqus calculates the hydrostatic pressure with reduced integration, first order elements such as the general-purpose continuum elements C3D8T, would result in a constant hydrostatic pressure throughout the whole element, and thus, using second order elements is imperative to obtain pressure gradients within an element. The second method relies on using the subroutine URDFIL, which enables obtaining pressure values from a previous increment during the analysis regardless of the type of elements used; this method has the drawback of relying on pressure stress values from the previous increment. In this work, the former method was adopted and hence, quadratic elements were adopted to discretize the geometry.

The computation of the pressure gradient requires the inverse of the Jacobian matrix. The simulations were carried out using 20-node quadratic hexahedral elements with reduced integration and hybrid linear pressure C3D20RT. These elements have eight (Gauss) integration points with their shape function in terms of the base (isoparametric) coordinates $\boldsymbol{\xi}$: (ξ, η, μ) for element e given by

$$N_i^e = \frac{1}{8}(1 + \xi\xi_i)(1 + \eta\eta_i)(1 + \mu\mu_i) \qquad 27$$

where $i = 8$. For simplicity the superscript e will be dropped throughout the rest of the text.

The coefficients (ξ_i, η_i, μ_i) of the base coordinate system $\boldsymbol{\xi}$ may be obtained from the coefficients (x_i, y_i, z_i) of the global Cartesian coordinates $\mathbf{x}$: (x, y, z) as follows:

$$\xi_i = \frac{x_i}{a}, \qquad \eta_i = \frac{y_i}{b}, \qquad \mu_i = \frac{z_i}{c} \tag{28}$$

where a, b, and c are the half edge lengths. The partial derivative of the shape function with respect to the base coordinates $(\frac{\partial N_i}{\partial \xi})$ is given by

$$\frac{\partial N_i}{\partial \xi} = \frac{1}{8} \xi_i (1 + \eta \eta_i)(1 + \mu \mu_i)$$

$$\frac{\partial N_i}{\partial \eta} = \frac{1}{8} \eta_i (1 + \xi \xi_i)(1 + \mu \mu_i) \tag{29}$$

$$\frac{\partial N_i}{\partial \mu} = \frac{1}{8} \mu_i (1 + \xi \xi_i)(1 + \eta \eta_i)$$

The partial derivative of the Cartesian coordinate with respect to the base coordinates $(\frac{\partial \mathbf{x}}{\partial \boldsymbol{\xi}})$ is given by

$$\frac{\partial x}{\partial \xi} = \sum_{i=1}^{8} x_i \frac{\partial N_i}{\partial \xi}, \qquad \frac{\partial x}{\partial \eta} = \sum_{i=1}^{8} x_i \frac{\partial N_i}{\partial \eta},$$

$$\frac{\partial x}{\partial \mu} = \sum_{i=1}^{8} x_i \frac{\partial N_i}{\partial \mu}$$

$$\frac{\partial y}{\partial \xi} = \sum_{i=1}^{8} y_i \frac{\partial N_i}{\partial \xi}, \qquad \frac{\partial y}{\partial \eta} = \sum_{i=1}^{8} y_i \frac{\partial N_i}{\partial \eta},$$

$$\frac{\partial y}{\partial \mu} = \sum_{i=1}^{8} y_i \frac{\partial N_i}{\partial \mu} \tag{30}$$

$$\frac{\partial z}{\partial \xi} = \sum_{i=1}^{8} z_i \frac{\partial N_i}{\partial \xi}, \qquad \frac{\partial z}{\partial \eta} = \sum_{i=1}^{8} z_i \frac{\partial N_i}{\partial \eta},$$

$$\frac{\partial z}{\partial \mu} = \sum_{i=1}^{8} z_i \frac{\partial N_i}{\partial \mu}$$

which in turn yields the Jacobian matrix $\mathbf{J}$ of $\mathbf{x}$ with respect to $\boldsymbol{\xi}$

$$\mathbf{J} = \begin{bmatrix} \dfrac{\partial x}{\partial \xi} & \dfrac{\partial y}{\partial \xi} & \dfrac{\partial z}{\partial \xi} \\[2mm] \dfrac{\partial x}{\partial \eta} & \dfrac{\partial y}{\partial \eta} & \dfrac{\partial z}{\partial \eta} \\[2mm] \dfrac{\partial x}{\partial \mu} & \dfrac{\partial y}{\partial \mu} & \dfrac{\partial z}{\partial \mu} \end{bmatrix} \qquad 31$$

The partial derivatives of the hexahedron shape functions with respect to Cartesian coordinates ($\frac{\partial N_i}{\partial \mathbf{x}}$) are given by

$$\frac{\partial N_i}{\partial x} = \frac{\partial N_i}{\partial \xi}\frac{\partial \xi}{\partial x} + \frac{\partial N_i}{\partial \eta}\frac{\partial \eta}{\partial x} + \frac{\partial N_i}{\partial \mu}\frac{\partial \mu}{\partial x}$$

$$\frac{\partial N_i}{\partial y} = \frac{\partial N_i}{\partial \xi}\frac{\partial \xi}{\partial y} + \frac{\partial N_i}{\partial \eta}\frac{\partial \eta}{\partial y} + \frac{\partial N_i}{\partial \mu}\frac{\partial \mu}{\partial y} \qquad 32$$

$$\frac{\partial N_i}{\partial z} = \frac{\partial N_i}{\partial \xi}\frac{\partial \xi}{\partial z} + \frac{\partial N_i}{\partial \eta}\frac{\partial \eta}{\partial z} + \frac{\partial N_i}{\partial \mu}\frac{\partial \mu}{\partial y}$$

which can be obtained by finding the numerically-inverted Jacobian matrix and multiplying it by the partial derivative of the shape function with respect to the base coordinates ($\frac{\partial N_i}{\partial \boldsymbol{\xi}}$) as follows

$$\begin{bmatrix} \dfrac{\partial N_i}{\partial x} \\[2mm] \dfrac{\partial N_i}{\partial y} \\[2mm] \dfrac{\partial N_i}{\partial z} \end{bmatrix} = \mathbf{J}^{-1} \begin{bmatrix} \dfrac{\partial N_i}{\partial \xi} \\[2mm] \dfrac{\partial N_i}{\partial \eta} \\[2mm] \dfrac{\partial N_i}{\partial \mu} \end{bmatrix} \qquad 33$$

In order to obtain the gradient of hydrostatic stress ($\nabla \sigma_h$) required for the calculation of diffusion flux, the partial derivative of hydrostatic stress with respect to the base coordinates ($\frac{\partial \sigma_h}{\partial \boldsymbol{\xi}}$) must be calculated as follows

$$\frac{\partial \sigma_h}{\partial \xi} = \sum_{i=1}^{8} \sigma_{h,i}\frac{\partial N_i}{\partial \xi}, \qquad \frac{\partial \sigma_h}{\partial \eta} = \sum_{i=1}^{8} \sigma_{h,i}\frac{\partial N_i}{\partial \eta},$$

$$\frac{\partial \sigma_h}{\partial \mu} = \sum_{i=1}^{8} \sigma_{h,i}\frac{\partial N_i}{\partial \mu} \qquad 34$$

and hence

$$\nabla\sigma_h = \frac{\partial\sigma_h}{\partial\boldsymbol{\xi}} \cdot \mathbf{J}^{-1}$$

3.4. Model verification

In order to verify the results obtained from the developed constitutive material model, its results were compared to benchmark numerical solutions provided by Abaqus [49]. Both, the mechanical response and the concentration-driven diffusion behavior, were evaluated against Abaqus built-in models. The stress-assisted diffusion (first term in Eq. 14) was verified by conducting a sequential mechanical-diffusion simulation using the Abaqus built-in diffusion model after defining the constant that controls the diffusion driven by gradients of equivalent pressure. The trapping of hydrogen in dislocation sites was tested against calculated values. The outcome of all verification steps yielded almost identical results.

3.4.1. Reference model

The mechanical response of the developed finite element model was compared to a three-dimensional model of the bearing 81104-TV, which will be referred to as "reference model" throughout the remainder of this article. It also served to deliver more accurate results pertaining to stress distribution and slip in the presence of friction in rolling contact. The reference model was run as a quasi-static system in Abaqus/Standard. Its geometry was simplified to consist of two washers and four rolling elements separated by a polyamide (PA-66) cage, Figure 3. Four rollers is the smallest number needed to make the system mechanically stable by relying on contact constraints and without adding constraints in the form of boundary conditions.
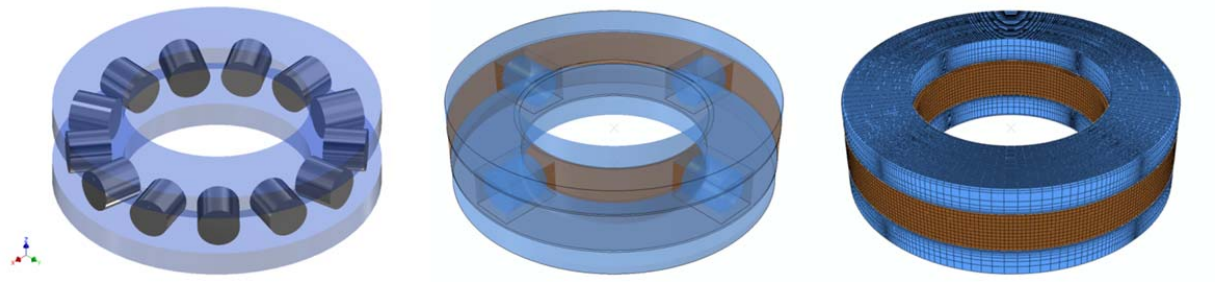
Figure 3. Overview of the reference model for 81104-TV

Abaqus built-in mechanical constitutive models were used for steel (elastic-plastic with kinematic hardening behavior; material parameters listed in Table 1) and PA-66 (elastic behavior with an elastic modulus of 3.95 GPa and Poisson's ratio of 0.39). Coulomb friction with a constant coefficient of friction (COF) of $\mu = 0.005$ was adopted based on an average value determined through a series of measurements carried out using the thrust-bearing tribometer, refer to Section 5.2. 20-node second-order hexahedral elements (C3D20) with displacement degrees of freedom were used to discretize the geometry. A fine mesh was used to discretize the contact zones with an average element size of 100×50×50 [μm]. Rotation boundary conditions and a normal load of 3.2 kN were applied to the upper ring while constraining the lower one. The lower ring was rotated five degrees to obtain the desired stress state.

4. Experimental Analysis

The experimental program in this study was conducted to obtain data needed as input to the numerical simulations and to run actual component tests capable of reproducing material damage under specific parameters.

4.1. Mechanical behavior of 100Cr6

Tensile tests were carried out to study the mechanical behavior of 100Cr6. The samples were fabricated from cold rolled 100Cr6 sheet metal hardened to 60 HRC with dimensions in accordance with DIN 50125 H 20×80 [50]. The displacement was measured using an extensometer with an initial gauge

length of 80 mm. The tests were carried out by applying the force along and perpendicular to the rolling direction of the sheet metal.

4.2. Rolling-contact fatigue

Rolling contact fatigue (RCF) tests were carried out using a customized bearing test rig, which has been used in previous studies [11]. FAG 81104-TV CRTBs were tested with a commercially-available fully additivated transmission oil ($KV_{40\,°C}$=64.0 mm^2/s, $KV_{100\,°C}$=9.5 mm^2/s). The elemental composition of the bearing steel 100Cr6 was analyzed in [10] by glow discharge optical emission spectroscopy (GDOES); the composition is given in Table 3. Its microstructure was analyzed in similar bearings [51] and was found to consist mainly of tempered martensite, homogeneously distributed primary spheroidized carbides $(Fe,Cr)_3C$, tempered carbides and approximately 10-12% retained austenite.

Table 3: Elemental composition of bearing steel 100Cr6 [10]

Cr	C	Mn	Si	Mo	V	Fe
1.52±0.03	1.08±0.02	0.33±0.02	0.26±0.03	< 0.1	< 0.1	balance

The tests were carried out with a normal load of 8 kN, at a speed of 700 rpm and a lubricant temperature of 90 °C. The test rig provides independent control of these parameters. During the test, the torque is measured by a torque cell, by which the coefficient of friction (COF) is obtained. Two sets of experiments with test durations of 25 h and 50 h were conducted. Any point on the roller has an over-rolling frequency factor of 2.9528 [41], and hence, each point on the roller undergoes approximately 6.2×10^6 and 12.4×10^6 load cycles for the 25.0 h and 50 h tests, respectively. Each test was repeated twice using a bearing from which three rollers were removed prior to testing to perform base hydrogen concentration measurements, thus, resulting in 40 tested rollers for post experimental analysis. It should be pointed out that a quantitative lifetime analysis of the bearings was not within the scope of the current work.

Rheological measurements were conducted on virgin and used samples of the lubricant at 90 °C to analyze and record any changes in its viscosity after running the RCF tests.

Following the RCF tests, the damage was observed by means of cross-sectional microscopy. For this purpose, a serial cross-sectioning procedure was carried out as depicted in Figure 4.
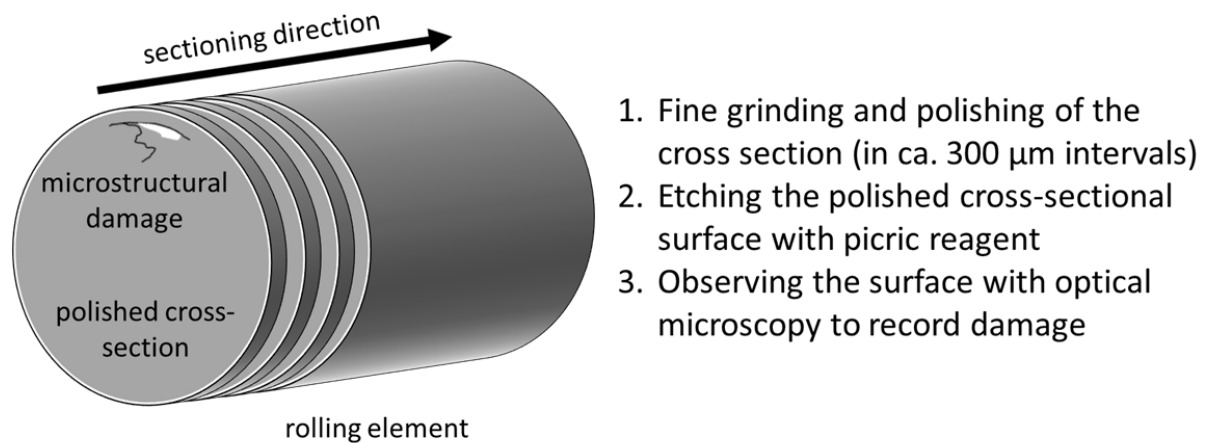

Figure 4. Illustration of the serial cross sectioning procedure

The integral hydrogen content of the rollers was determined by means of carrier gas hot extraction. By melting the sample, this method releases both trapped and diffused hydrogen. The hydrogen analyzer was calibrated using 1.5 ± 0.25 ppm hydrogen standard samples. Reference values of the hydrogen content trapped in the bearing steel in its virgin state was obtained from the three rollers removed from each bearing prior to testing. The difference in hydrogen content was measured from at least three tested rollers from each bearing directly after completing each RCF test. The selection of this bearing size enabled analyzing whole rollers in the carrier gas hot extraction analyzer without the need of any cutting or preparation procedure and thus, eliminating their influence on the measured values. The custom built test rig also enabled disassembling the tested bearings in a very short time to avoid any hydrogen release after the test; the samples were submerged in liquid nitrogen before being analyzed. Moreover, to eliminate any possible influence of trapped lubricant on the measured concentrations, only samples with no surface damage were selected after being degreased with acetone and n-hexane and carefully removing any lubricant/oxide/recast layer by slightly grinding off the surface with emery paper. Failing to

perform proper cleaning of the sample surface prior to the analysis has proven to result in unrealistic spikes of hydrogen concentration.

5. Results

5.1. Mechanical behavior of 100Cr6

The stress strain curves obtained from the tensile tests along and perpendicular to the rolling direction are shown in Figure 5.

The initial yield strength measured along the rolling direction was found to be 1187.6 MPa at a total strain of 0.006 (the onset of deviation from the linear stress-strain response); the hardening modulus was found to be 184.25 GPa. The tests carried out perpendicular to the rolling direction resulted in an initial yield strength of 1202.5 MPa at a total strain of 0.006; the hardening modulus was found to be 186.75 GPa. Average values of these measurements (σ_0=1195.1 MPa and H=185.5 GPa) were adopted in the numerical model.

(a)   (b)
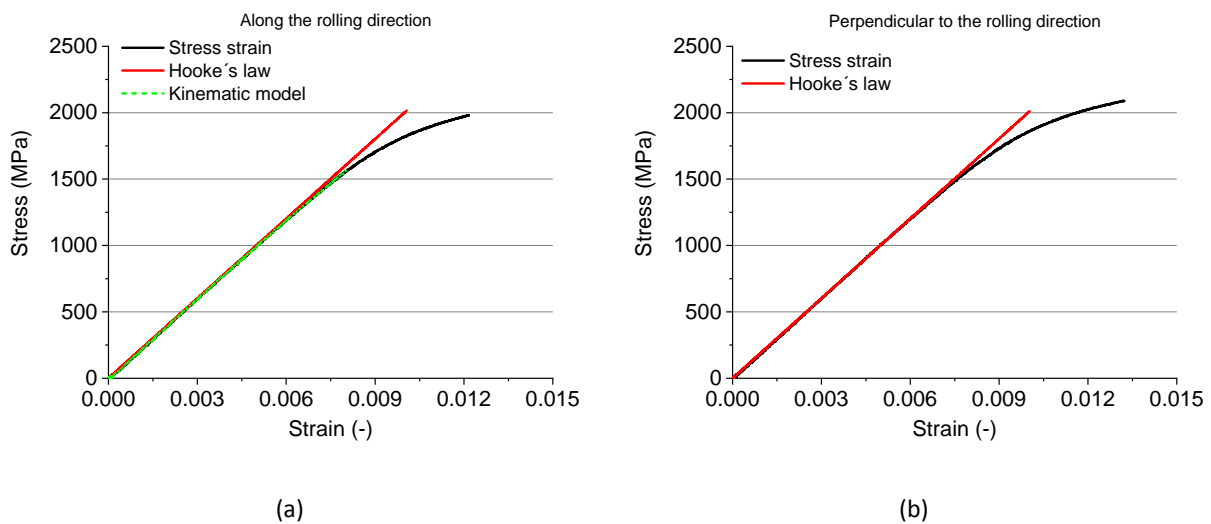
Figure 5. True stress-strain curves of 100Cr6 (a) along the rolling direction and (b) and perpendicular to the rolling

5.2. Rolling contact tests

The COF profile plotted against test duration for all four tests is shown in Figure 6. The COF decreases to an almost steady-state value after approx. 30 h. It should be noted that the COF of roller bearings, such as that recorded during the RCF tests and shown in Figure 6, has many sources and hence, does not follow the exact definition of the Coulomb friction coefficient.
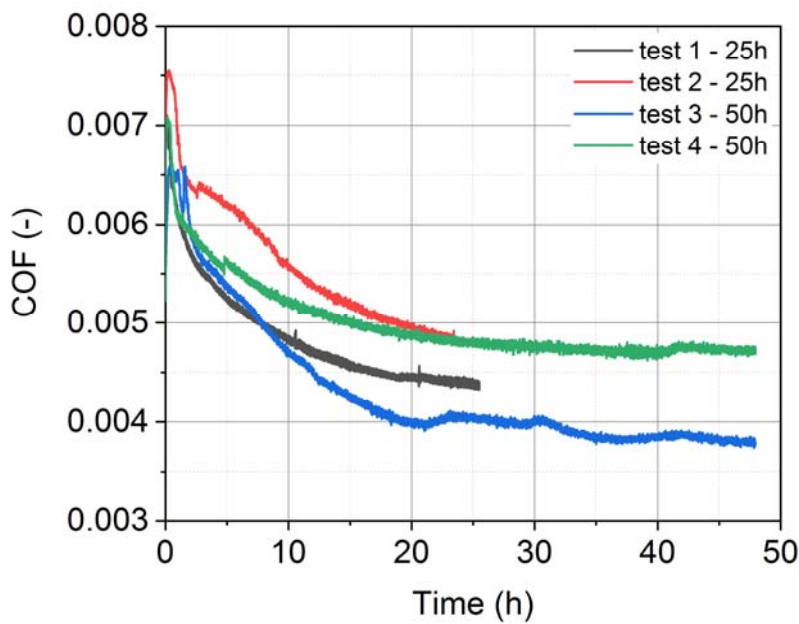

Figure 6. COF against time recorded during the RCF tests

The rheological measurements on virgin samples of the lubricant resulted in a dynamic viscosity of 0.0087 Pa·s at 90 °C, which is consistent with the value reported by the manufacturer. The analysis of used samples of the lubricant indicated an insignificant change in viscosity after the 25 h RCF tests and about 10% reduction after the 50 h tests.

The bearings tested for 25 h survived without showing any signs of damage. On the other hand, close to 50 h running time, the bearings started showing indication of failure demonstrated by increased vibrations. In addition to surface damage in the form of flaking, serial cross-sectional optical microscopy inspection of the 50-h tested rollers revealed subsurface damage as shown in Figure 7.
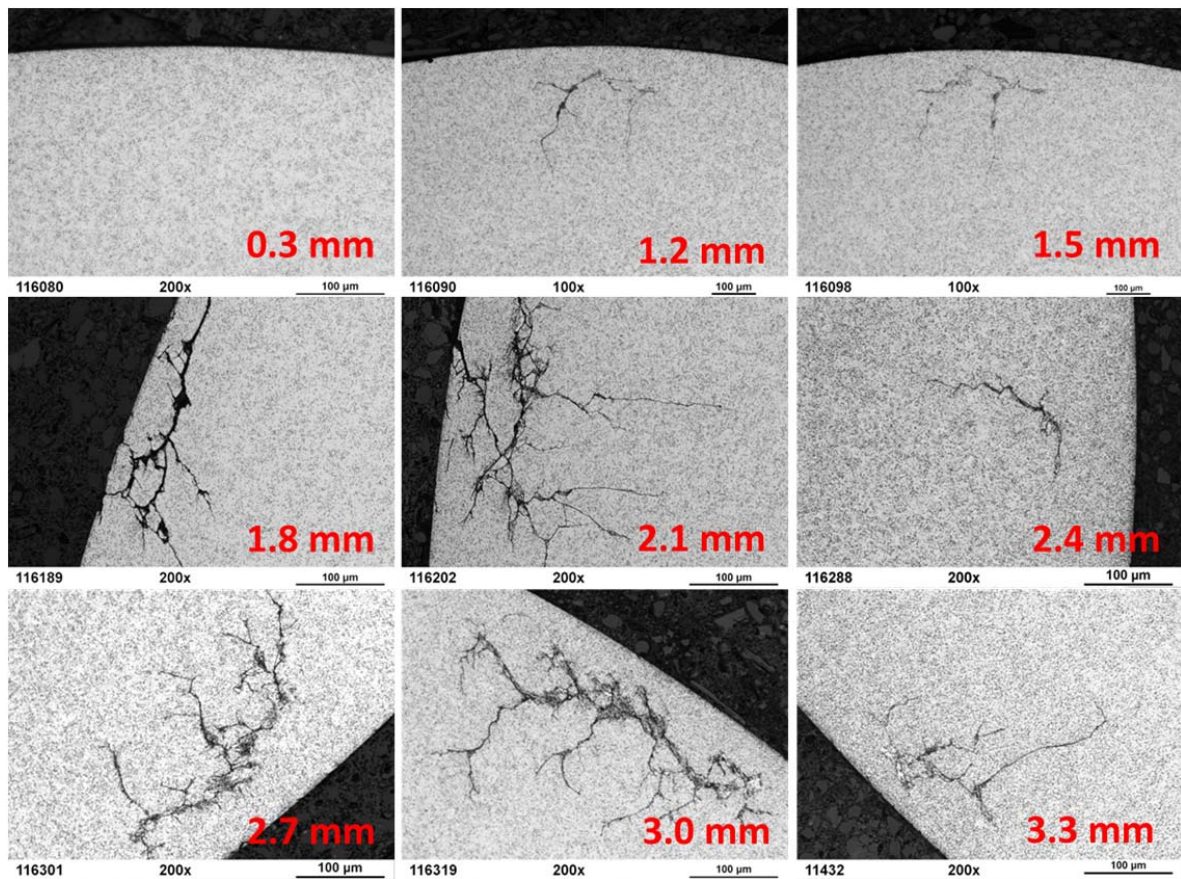
Figure 7. Cross-sectional optical micrographs of a roller sectioned along its axis with the axial position indicated in each image. WEC networks appear in the subsurface region after the 50 h tests

Subsurface crack networks (WEC) associated with WEA have formed below the of roller surfaces at depths of in between 10 µm and 400 µm, Figure 7 and Figure 8. WEA were found between 10 µm and 180 µm below the surface. In some cases, crack propagation breached the surface causing flaking.
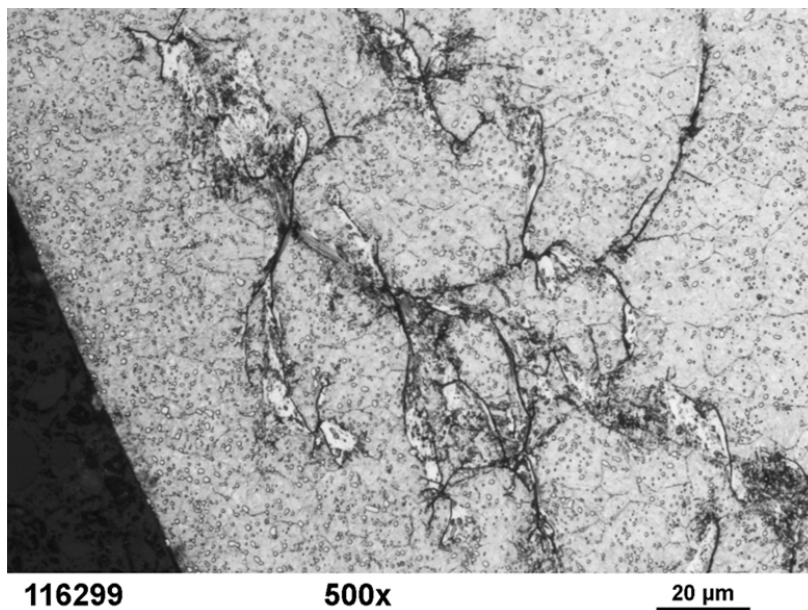
Figure 8. Optical micrograph showing WECs and WEA in the subsurface region of a roller after a 50 h test

The carrier gas hot extraction analysis results are shown for all tests in Figure 9.
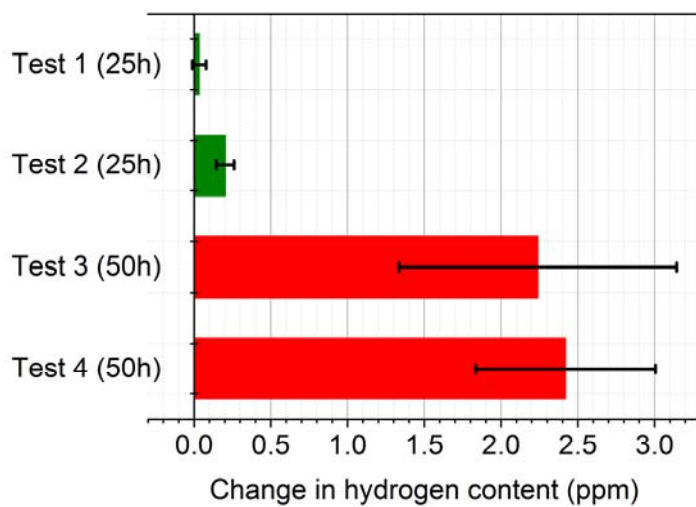
Figure 9. Change in measured hydrogen content of the rollers as a result of RCF tests

Compared to the hydrogen content found in virgin samples (mean value approx. 1.1 ppm), a significant increase was observed only after the 50 h RCF tests.

5.3. Simulations

5.3.1. Diffusion under bearing contact

The von Mises stress showed a maximum value of ~1.6 GPa appearing 300 µm from the edges of the roller. A weaker subsurface peak von Mises stress of 1100 MPa appeared in the center of the roller almost 50 µm below the surface, Figure 10a. The reference model showed almost identical results (both magnitude and location) with a peak von Mises stress of ~1.5 GPa and a slightly higher subsurface peak of 1200 MPa, Figure 10b. The Hertzian contact solution based on a two-dimensional cylinder-on-flat half-space contact results in a peak von Mises stress of ~1.0 GPa at a distance of 55 µm below the surface. It is worth pointing out that this stress state is sensitive to any changes in the dimensions of the fillet and the crown radius.
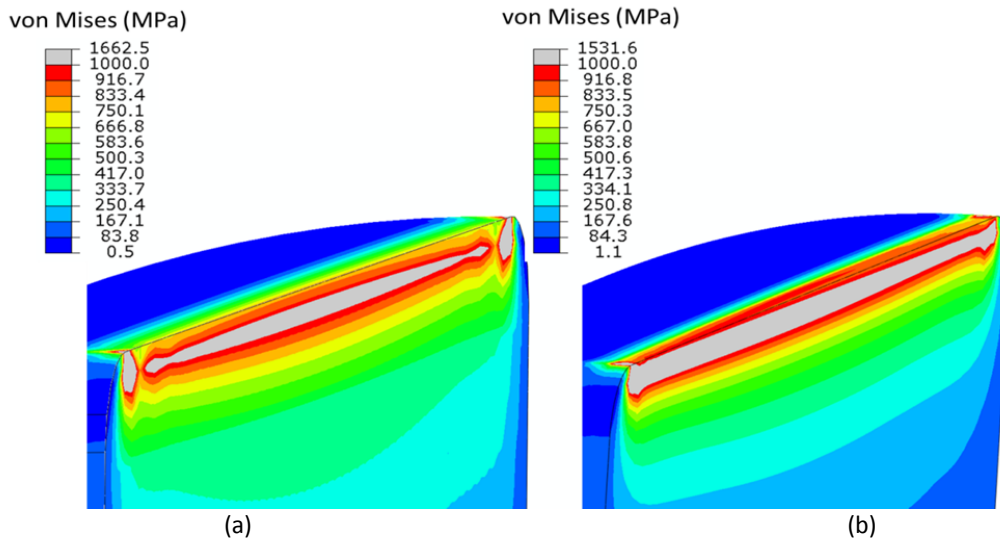
Figure 10. von Mises stress distribution through a cross section (a) coupled diffusion model; (b) reference model; σ_0 = 1195.1 MPa

Plastic strains, with a maximum value of ϵ^{pl}=1.9×10^{-3}, appeared on the surface at the location of maximum von Mises stress, Figure 11a; almost no subsurface plastic deformation occurs. The trapped hydrogen distribution coincided with that of the equivalent plastic strain, Figure 11b. The value of the ratio of trapped hydrogen concentration in dislocations normalized to the surface hydrogen concentration (C_T/C_S) amounted to 5.8×10^{-4} after 50 h. In the absence of plastic deformation the value of

C_T/C_S = 2.9×10^{-5}, which corresponds to the trapped hydrogen concentration in the dislocations in the annealed material having $\vartheta = \vartheta_0$ (according to Eq. 6).
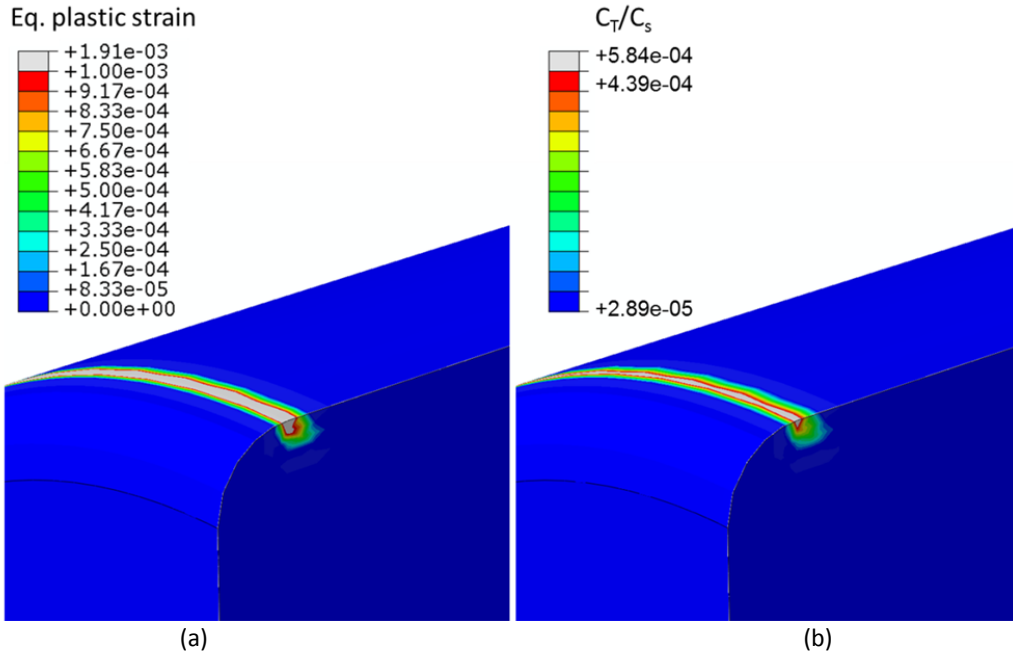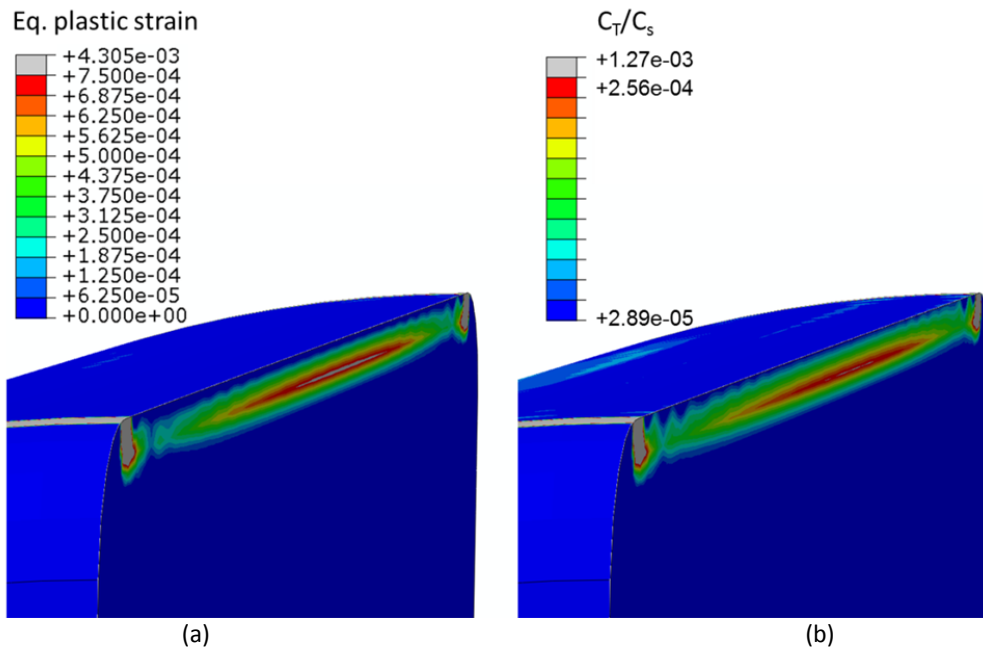

Figure 11. (a) Equivalent plastic strain distribution in the roller; (b) ratio of trapped hydrogen concentration to surface hydrogen concentration; σ_0 = 1195.1 MPa

When modeling the system with reduced initial yield strength (σ_{0-red} = 1000 MPa), the maximum equivalent plastic strain amounts to ϵ^{pl}=4.3×10^{-3} (on the surface at the edges of the rollers, Figure 12a) which raised C_T/C_S to 1.3×10^{-3}, Figure 12b. The formation of subsurface (i.e., fully-contained) plastic deformation at the location of peak subsurface equivalent von Mises stress resulted in hydrogen trapping with a concentration ratio of C_T/C_S=2.6×10^{-4}. It should be pointed out that the total hydrogen concentration after 50 h for both cases: σ_0 = 1195.1 MPa and σ_{0-red} = 1000.0 MPa revealed almost identical distributions with a disparity pertaining to trapped hydrogen.

Figure 12. (a) Equivalent plastic strain distribution in the roller; (b) ratio of trapped hydrogen concentration to surface hydrogen concentration σ_{0-red} = 1000.0 MPa

The distribution of the hydrostatic stress[1] upon initial contact is shown along with the distribution of normalized total hydrogen concentration.
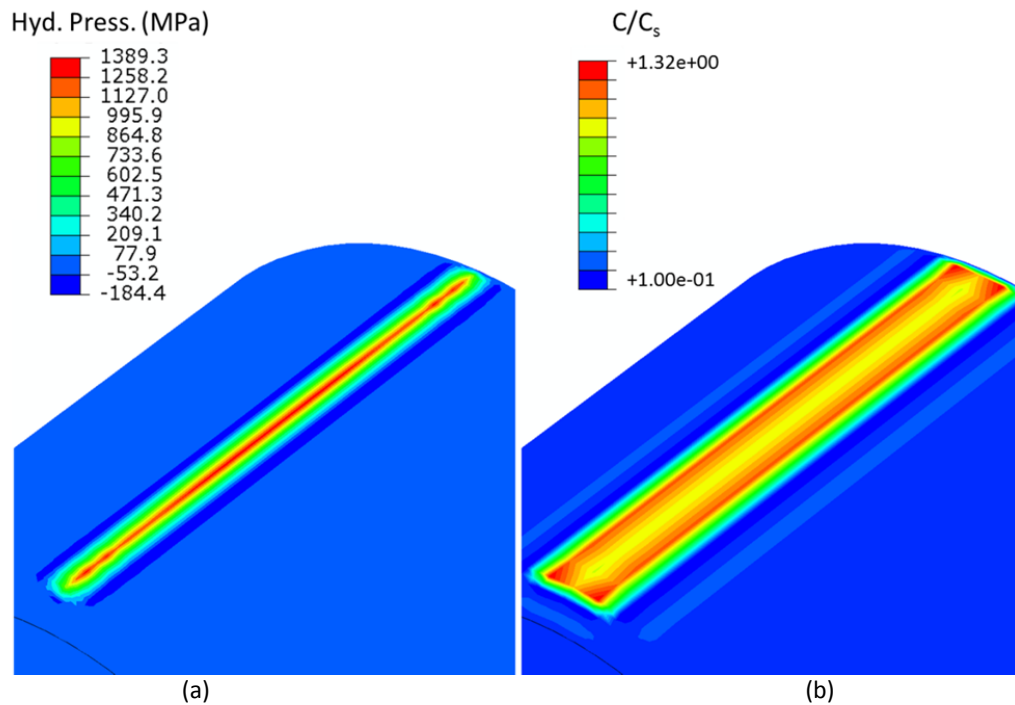

Figure 13. (a) Hydrostatic pressure distribution; (b) ratio of total hydrogen concentration to surface hydrogen concentration upon initial contact

---

[1] Only in the case of hydrostatic stress, Abaqus assigns a positive sign for compression and a negative for tension.

During rolling contact, the distribution of the maximum principal stress (S_{max}) is shown in Figure 14a (obtained from the reference model). Asymmetry in the value of the tensile stress appears during rolling contact due to surface tractions. Figure 14b shows S_{max} plotted against two paths in the axial direction.
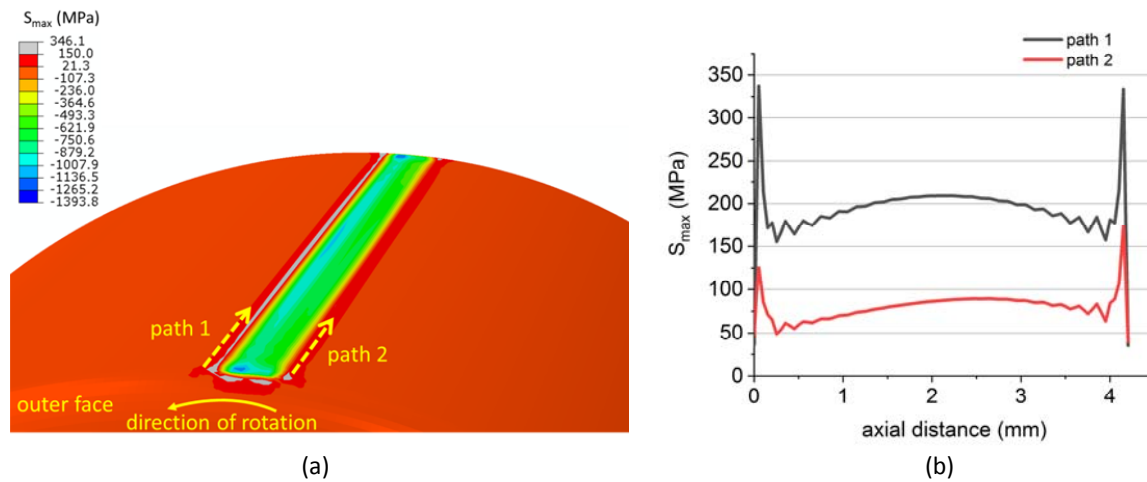

(a)   (b)

Figure 14. (a) Maximum principal stress distribution on the surface of a roller; (b) S_{max} along two axial paths; zero in axial distance refers to the outer face of the roller (reference model)

The normalized diffused hydrogen concentration along radial paths was plotted at the center and the edge of the roller, Figure 15. The curves indicate slightly higher concentration of hydrogen towards the center of the roller; the initial portion of the curve appears concave downward indicating slight accumulation of hydrogen in the initial 200 µm below the surface.

5.3.2. The influence of residual stresses

The simulations of hydrogen diffusion with implemented residual stress fields were carried out for the three distinct cases: (i) w/o residual stress, (ii) C-T and (iii) C-T-C (refer to Section 3.2.2).
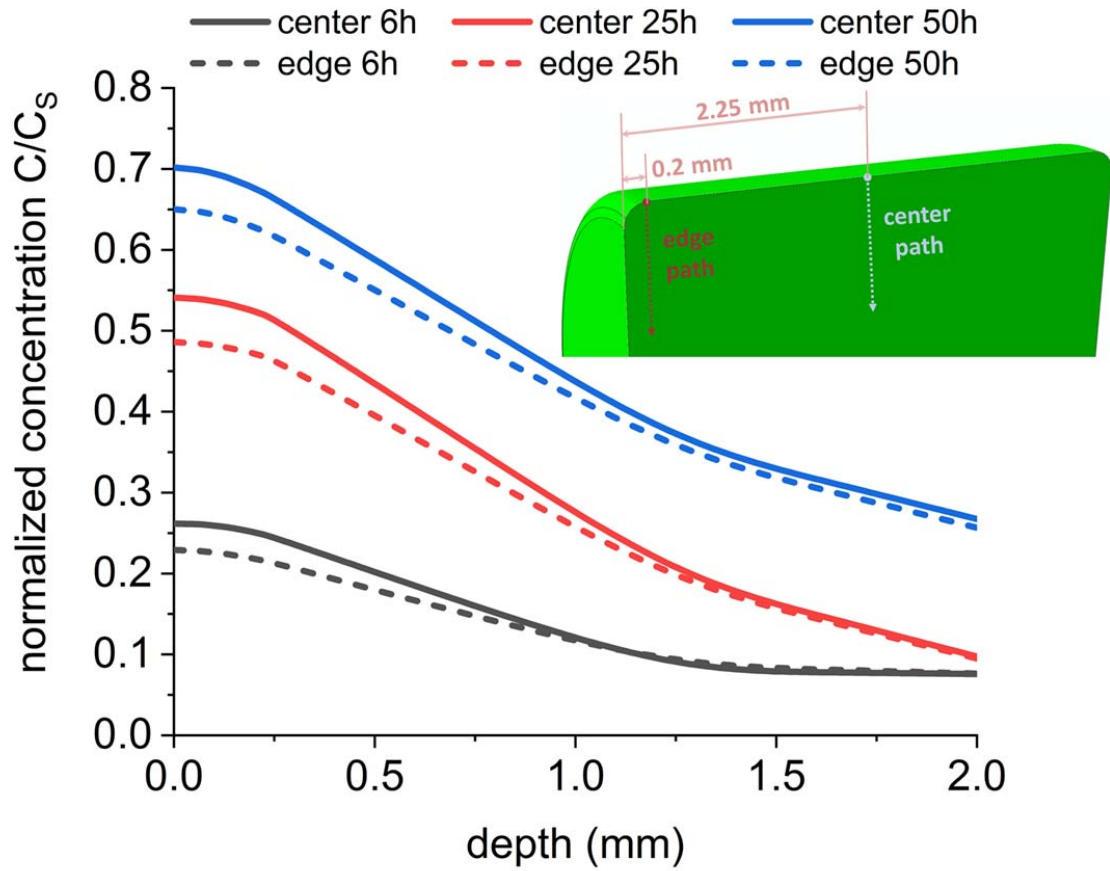
Figure 15. Total normalized hydrogen concentration in the depth plotted along the center and edge paths of the roller

For the case w/o residual stress, the normalized concentration curve "C/C_0 w/o residual stress" in Figure 16 shows a declining concentration in the depth as expected from a concentration-driven diffusion. A comparison of this curve with the concentration curves obtained from the rolling contact simulations (shown in Figure 15) shows the effect of stress-driven diffusion on the hydrogen concentration profile in the depth. While in both cases the concentration generally decreases by increasing depth, in the near surface area, the former appears concave upward (concentration-driven diffusion) whereas the latter is concave downward (combined concentration-driven and stress-assisted diffusion), see Figure 17.
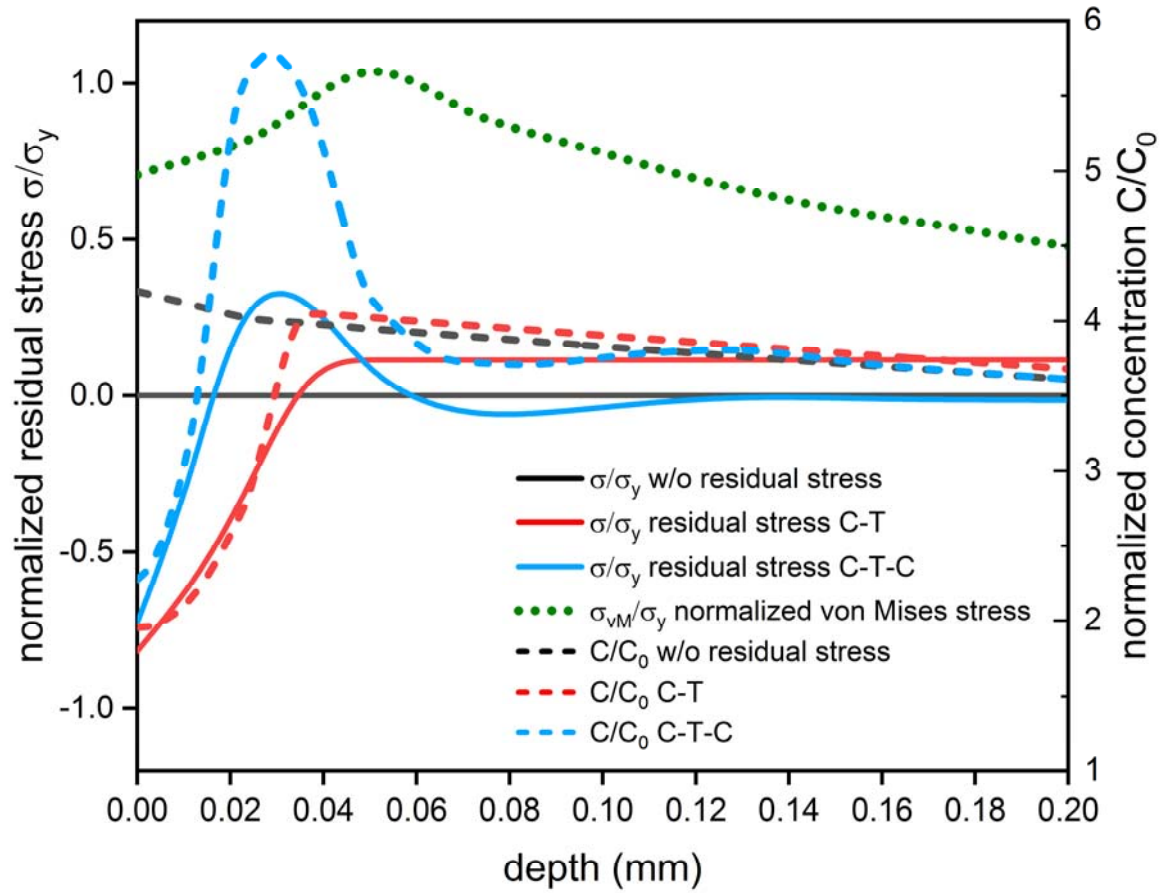
Figure 16. Normalized hydrogen concentration in the depth plotted along a radial path from the center of the roller for three distinct residual stress profiles

When a compression-tension residual stress field in the case C-T was implemented (this corresponds to the residual stress observed in a through-hardened roller in its virgin state), hydrogen appears to be repelled off the surface and into the depth (curve C/C_0 C-T), in which it shows a somehow rather slight elevation in concentration in comparison to the residual stress free case. Here it should be pointed out that a fivefold decrease in the value of tensile residual stress did not show any significant influence on the value of subsurface hydrogen concentration. In other words, the ratio of maximum compression to maximum tension had an insignificant effect on the peak hydrogen concentration, Figure 18a.
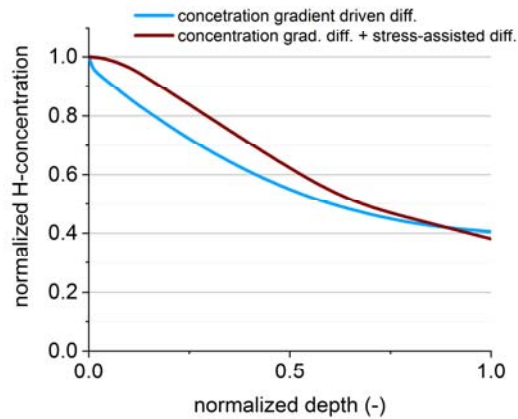
Figure 17. Normalized hydrogen concentration in the depth plotted along a radial path from the center of the roller for concentration gradient driven diffusion and combined concentration gradient driven and stress-assisted diffusion

The third case (C-T-C), by which subsurface residual stresses are transformed from tension into compression under the influence of cumulative subsurface plastic deformation, shows a distinct behavior. Here it appears that hydrogen is repelled from both compressive stress fields (directly on the surface and close to the maximum von Mises stress) and accumulated within the zone of tensile residual stress. The hydrogen concentration, for this case, shows a peak at approx. 30 μm below the surface. It is also important to notice that in the case C-T-C, reducing the tensile stress in the center to a lower value, or even substituting it by a weak compressive stress (abbreviated C-c-C in Figure 18b), results in the same trend. In other words, hydrogen accumulation occurs towards the direction of positive hydrostatic stress gradient.

6. Discussion

The post-RCF cross-sectional analysis, Figure 7, revealed crack initiation in the subsurface region without signs of classical fatigue degradation in steel (i.e., dark etching regions or zones of subsurface microcracks). The damage observed in the bearings could not be fully explained merely due to hydrogen-assisted diffusion under tribological contact; the simulations showed slight subsurface accumulation of
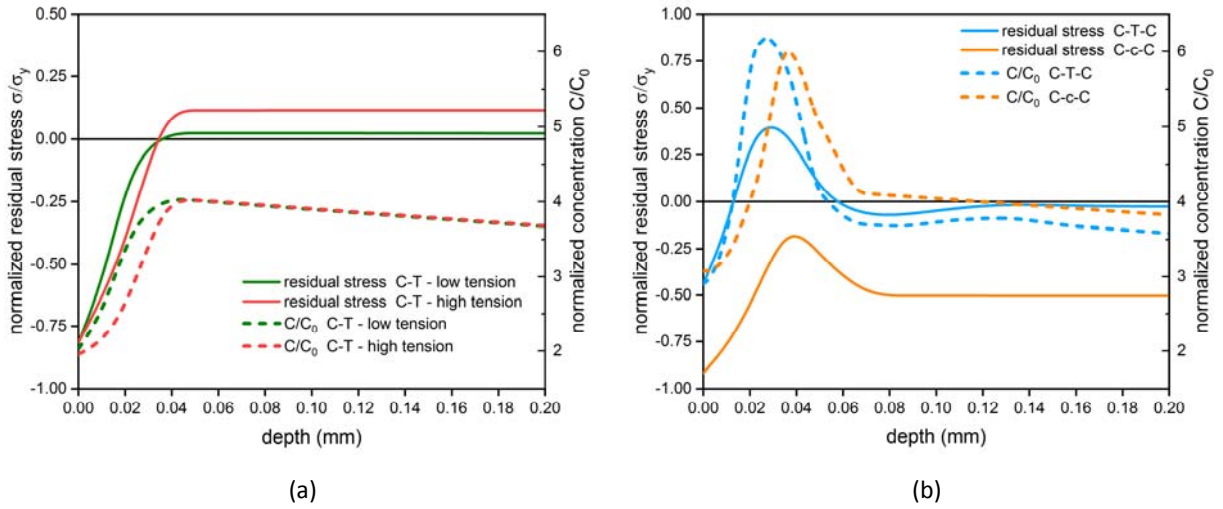
Figure 18. Total normalized hydrogen concentration in the depth plotted along a radial path from the center of the roller for (a) C-T with different tension stresses, (b) C-T-C with weak compressive stress in the between two higher compress stress fields, i.e., C-c-C

hydrogen due to tribological loading, Figure 15, which is in line with the findings of Winzer and Khader [16] and Kadin [17]. On the other hand, and in addition to altering the stress state in the material, plastic deformation causes an increase in hydrogen traps density due to dislocation multiplication. The concentration of trapped hydrogen (C_T) coincided with the distribution of accumulated plastic strain. Nevertheless, plastic strains remained small and, thus, resulted in very low concentrations of trapped hydrogen in comparison to the diffusive hydrogen concentration (C_L). The subsurface plastic deformation observed in the model with reduced yield strength (σ_{0-red} = 1000.0 MPa) led to hydrogen trapping below the surface, however, the trapped hydrogen remained insignificant in affecting the total hydrogen concentration. This is attributed to the low ductility of martensitic steel 100Cr6. The effect of the number of trap sites per Burgers vector on the total hydrogen concentration in rolling-sliding contact was addressed in [16], and it was concluded that the accumulation of hydrogen was mainly defined by the equilibrium concentration of trapped hydrogen at deformation-induced defects. It should be noted, however, that the trapping model adopted in this study considers dislocations as the only source of traps in the system.

Nevertheless, there is strong evidence that points out to the role played by specific distributions of surface and subsurface residual stresses, wherein diffusible hydrogen appears to accumulate and shows a peak just above the region of highest von Mises stress, Figure 16. The presence of near surface residual stresses along with the accumulation of subsurface plastic deformation resulted in preferential zones for hydrogen to accumulate through stress-assisted diffusion. Within this context, the tribological contact, being the main culprit of lubricant degradation that provides a hydrogen source, resulted in plastic strains which modified the subsurface residual stress distribution. The cyclic loading and the corresponding accumulation of subsurface plastic strains (in a fully-contained plastic deformation mode), which can be described by ratcheting, results in altering the residual stress profile in the depth from compression at the surface layers and tension further down in the depth (C-T) to compression followed by tension followed by another compression field further in the depth (C-T-C). This particular stress profile (or any residual stress profile that involves having a tensile, or a weak compressive, hydrostatic stress field in between two stronger compressive stress fields, compare C-T-C and C-c-C in Figure 18b) triggers the accumulation of hydrogen in the tensile (or weak compressive) hydrostatic stress zone and may be correlated with the presence of WEC/WEA observed at the same depth with high density, see Figure 19. It is worth mentioning that a higher value of the partial molar volume of hydrogen ($\bar{V}_H$; refer to Eq. 14) would strengthen stress-assisted diffusion leading to more hydrogen transport in the direction of positive hydrostatic stress gradient (e.g., compression to tension) and consequently more subsurface accumulation. This zone may be thought of as a bottleneck or a barrier in the diffusion processes that leads to the accumulation of diffusible hydrogen and may be explained in light of the fact that stress-assisted diffusion is driven by stress gradients as it repels hydrogen away from strong compressive fields into weaker compressive (or tensile) fields. This is supported by literature findings that report the large majority of WEC occurrences (i) at rather moderate contact stresses [52, 53, 54, 55, 56] that are not high enough to extend the plasticity zone in the material to its surface in an "uncontained plastic deformation
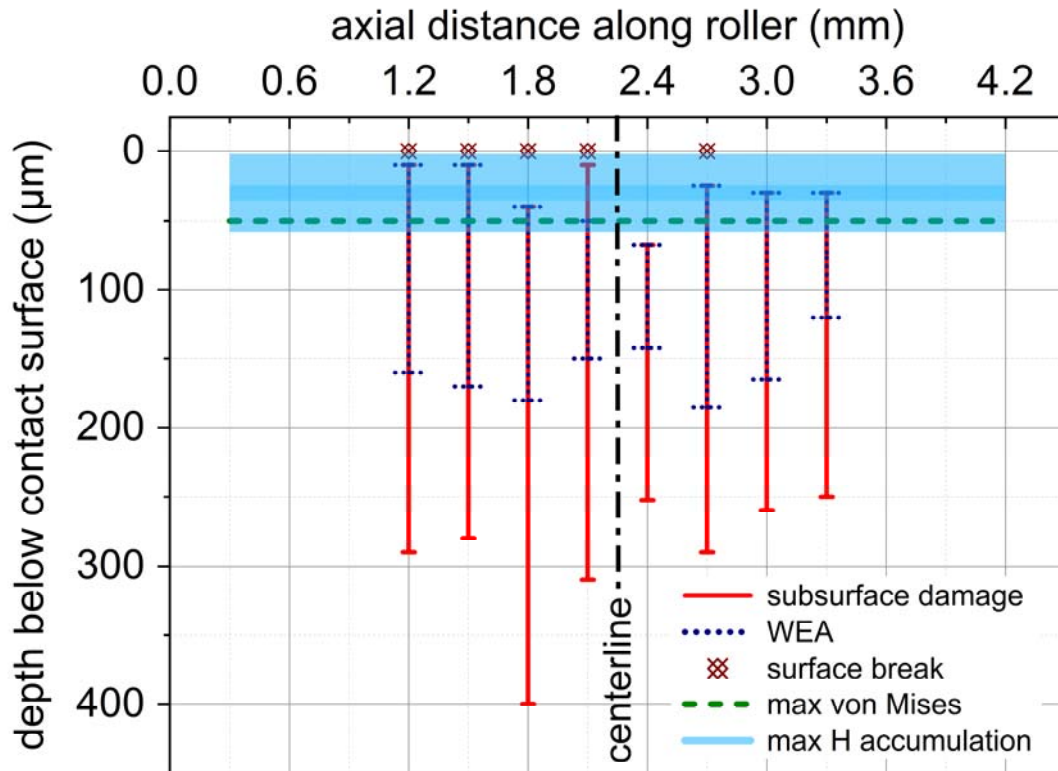
Figure 19. Subsurface distribution of damage and WEA

mode" and (ii) in through-hardened bearings [57] that exhibit a residual stress profile similar to what has been considered in this work. It should be pointed out that the gradual transformation of the stress profile from compression-tension to compression-tension-compression is dependent on the number of stress cycles and the degree of accumulated plastic deformation and hence, would explain the absence of damage in the short 25-h RCF tests. For instance, this behavior was observed by Voskamp et al. [28] as early as 10^6 revolutions which, given the over-rolling frequency factor of the bearing used in their study, amount to approx. 5.0×10^6 load cycles. On the other hand, if subsurface plastic deformation is introduced during the first few rotations (i.e., during the shakedown phase), a threshold hydrogen concentration for a ductile-to-brittle-transition may be required to trigger crack formation. It may be argued that a critical combination of mechanical stress and a certain degree of material degradation/embrittlement is required to prompt premature damage. For instance, the hydrogen content following the 25 h RCF tests (see Figure 9) is believed not to have reached a critical value to

cause enough degradation/embrittlement in steel and enable crack initiation, thus, explains the absence of WEC/WEA in these tests. It was argued by several researchers that 1-2 ppm [58, 59], or even slightly lower [60, 61], of diffusible hydrogen content resulted in premature failure of bearing steel.

When comparing the subsurface damage and the locations of hydrogen accumulation, it should be noticed that the computed stress state relies on a model of the material in its undamaged state. This also applies to the fields of residual stress implemented in the simulations. The presence of cracks results in substantial alteration to stresses and the resulting zone of accumulated hydrogen. Moreover, the distribution of residual stress may differ locally, thus resulting in changing the location of maximum accumulated hydrogen. Furthermore, an accurate knowledge of subsurface crack initiation sites is needed. In this analysis, the initiation sites were assumed to be the circumferential portion of the WEC. An earlier detection of damage may yield more accurate results of the locations of crack initiation sites. This information is also dependent on the increment of the serial sectioning procedure, which was about 300 μm in this work. A coarse cross sectioning results in a considerable margin of error for three-dimensional crack networks; the three-dimensional nature of WEC/WEA is shown in the work of Oezel et al. [58]. The density and distribution of WEC observed in the damaged rollers agree to a certain extent with the findings of Richardson et al. [62]. WEC density and distribution may be affected by several factors such as slip, friction and the localized film thickness (cf. Franke et al. [63]), the latter of which influences the degradation rate of the lubricant and the corresponding influx of hydrogen into steel. All of these factors combined shed a light on any possible disparity between the experimental and numerical results.

Tensile stresses act as drivers for cracks, especially in brittle/embrittled materials. The maximum principal stress (S_{max}) distribution revealed a peak on the roller surface (see Figure 14). The asymmetric distribution is due to surface tractions that modify the stress state at the leading and trailing edges of the contact. An eccentricity in the peak of S_{max}, either towards the outer or inner edge, may also occur

depending on the particular geometry of the roller and the corresponding contact configuration, slip between the roller and raceways or due to any misalignment in the bearing. Subsurface cracks would breach the material surface and cause flaking at regions of high tensile stress. It should be pointed out that both the magnitude of tensile stress and the affected volume play a decisive role in determining the most critical location at which a crack may break the surface. Similarly, volume defects, such as inclusions, are known to acts as nucleation sites for microcracks and have been even correlated with the formation of WEC (cf. Evans et al. [64]). The distribution of volume defects is of special interest in large bearings, which due to technical aspects pertaining to manufacturing, become inevitable and appear in relatively large numbers. It should be however mentioned that the rate and orientation of inclusions was found not to affect WEC formation mechanisms in angular contact ball bearing as argued in the work of Du Crehu [56]. Another aspect that was not treated in this work is the effect of hydrogen on the mechanical properties of the material, in other words effects such as hydrogen enhanced decohesion (HEDE) and hydrogen enhanced localized plasticity (HELP), which may contribute to changes in the stress state and consequently to the diffusion kinetics.

7. Summary

In this work a coupled diffusion-mechanical finite element simulation model was developed, verified and used to study stress-assisted diffusion in a CRTB. The outcome of the simulations was correlated with the results obtained from RCF experiments and hydrogen measurements. The following was concluded:

- Carrier gas hot extraction analysis indicated an increase in hydrogen content in all tested samples after conducting the RCF tests; the increase in hydrogen content was substantial for longer test durations (50 h tests)

- Damage in the form of subsurface networks of WEC and surface flaking was observed in the 50-h RCF tests; the 25-h tests did not result in any form of damage

- The coupled diffusion-mechanical simulations showed only minor hydrogen accumulation due to stress-assisted diffusion in comparison to concentration gradient driven diffusion

- It was found that particular residual stress distributions (tension in between two compressive stress fields or weak compression in between two stronger compression fields) in the material create preferential subsurface diffusible hydrogen accumulation sites; these residual stresses may be induced by heat treatment and are altered during operation by rolling contact and the accumulation of subsurface plastic deformation

- The experimentally-observed subsurface damage, in particular subsurface crack initiation sites associated with WEA, showed good agreement with the numerically-computed location of maximum subsurface hydrogen accumulation observed in the presence of residual stresses

Acknowledgment

References

[1] K. Tamada and H. Tanaka, "Occurrence of brittle flaking on bearings used for automotive electrical instruments and auxiliary devices," *Wear,* vol. 199, pp. 245-252, 1996.

[2] T. Bruce, E. Rounding, H. Long and R. Dwyer-Joyce, "Characterisation of white etching crack damage in wind turbine gearbox bearings," *Wear,* Vols. 338-339, pp. 164-177, 2015.

[3] B. Gould, A. Greco, K. Stadler and X. Xiao, "An Analysis of premature cracking associated with microstructural alterations in an ASIS 52100 failed wind turbine bearing using X-ray tomography," *Materials and Design,* no. 117, pp. 417-429, 2017.

[4] A. Greco, S. Sheng, J. Keller and A. Erdemir, "Material wear and fatigue in wind turbine Systems," *Wear,* vol. 302, pp. 1583-1591, 2013.

[5] H. Al-Tameemi, H. Long and R. Dwyer-Joyce, "Initiation of sub-surface micro-cracks and white etching areas from debonding at non-metallic inclusions in wind turbine gearbox bearing," *Wear,*

Vols. 406-407, pp. 22-32, 2018.

[6] M. Kohara, T. Kawamura and M. Egami, "Study on mechanism of hydrogen generation from lubricants," *Tribology Transactions,* vol. 49, pp. 53-60, 2006.

[7] R. Lu, I. Minami, H. Nanao and S. Mori, "Investigation of decomposition of hydrocarbon oil on the nascent surface of steel," *Tribology Letters,* vol. 27, no. 1, pp. 25-30, 2007.

[8] P. John, J. Cutler and J. Sanders, "Tribological behavior of a multialkylated cyclopentane oil under ultrahigh vacuum conditions," *Tribology Letters,* vol. 9, no. 3-4, pp. 167-173, 2001.

[9] D. Kuerten, N. Winzer, A. Kailer, W. Pfeifer, R. Spallek and M. Scherge, "In-situ detection of hydrogen evolution in a lubricated sliding pin on disk test under high vacuum," *Tribology International,* pp. 324-331, 2015.

[10] D. Kuerten, "Einfluss der tribochemischen Schmierstoffoxidation auf die wasserstoffinduzierte Wälzkontaktermüdung," vol. PhD Dissertation, Fraunhofer Verlag, 2015.

[11] D. Kürten, I. Khader, R. Raga, P. Casajús, N. Winzer, R. Spallek, M. Scherge and A. Kailer, "Hydrogen assisted rolling contact fatigue due to lubricant degradation and formation of white etching areas," *Engineering Failure Analysis,* vol. 99, pp. 330-342, 2019.

[12] P. Sofronis and R. M. McMeeking, "Numerical analysis of hydrogen transport near a blunting crack tip," *Journal of the Mechanics and Physics of Solids,* vol. 37, no. 3, p. 317–350, 1989.

[13] J. Lufrano, P. Sofronis and H. Birnbaum, "Modelling of hydrogen transport and elastically accommodated hydride formation near a crack tip," *Journal of the Mechanics and Physics of Solids,* vol. 44, no. 2, p. 1996, 179-205.

[14] A. Varias and A. Massih, "Hydride-induced embrittlement and fracture in metals—effect of stress and temperature distribution," *Journal of the Mechanics and Physics of Solids,* vol. 50, no. 7, p. 2002, 1469-1510.

[15] A. Krom, R. Koers and A. Bakkar, "Hydrogen transport near a blunting crack tip," *Journal of the Mechanics and Physics of Solids,* vol. 47, no. 4, pp. 971-992, 1999.

[16] N. Winzer and I. Khader, "Hydrogen diffusion and trapping in bodies undergoing rolling contact," *Wear,* vol. 303, no. 1-2, pp. 451-458, 2013.

[17] Y. Kadin, "Modeling of hydrogen transport in static and rolling contact," *Tribology Transactions,* vol. 58, no. 2, pp. 260-273, 2015.

[18] W. Kruhöffer and J. Loos, "WEC formation in rolling bearings under mixed friction: influences and "friction energy accumulation" as indicator," *Tribology Transactions,* vol. 60, no. 3, pp. 516-529,

2017.

[19] A. Díaz, J. Alegre and I. Cuesta, "A review on diffusion modelling in hydrogen related failures of metals," *Engineering Failure Analysis,* vol. 66, pp. 577-595, 2016.

[20] C.-S. Oh, Y.-J. Kim and K.-B. Yoon, "Coupled Analysis of Hydrogen Transport using ABAQUS," *Journal of Solid Mechanics and Materials Engineering,* vol. 4, no. 7, pp. 908-917, 2010.

[21] R. Falkenberg, Simulation von Wasserstofftransport und Rißwachstum infolge wasserstoffinduzierter Spannungsrißkorrosion mit einer Analyse der Kopplungsphänomenologie, vol. PhD Thesis, Kiel: Technischen Fakultät der Christian-Albrechts-Universität zu Kiel, 2010.

[22] O. Barrera, E. Tarleton, H. Tang and A. Cocks, "Modelling the coupling between hydrogen diffusion and the mechanical," *Computational Materials Science,* vol. 122, pp. 219-228, 2016.

[23] A. Díaz, J. Alegre and I. Cuesta, "Coupled hydrogen diffusion simulation using a heat transfer analogy," *International Journal of Mechanical Sciences,* Vols. 115-116, p. 2016, 2016.

[24] Y. Charles, H. T. Nguyen and M. Gaspérini, "Comparison of hydrogen transport through pre-deformed synthetic polycrystals and homogeneous samples by finite element analysis," *International Journal of Hydrogen Energy,* vol. 42, no. 31, pp. 20336-20350, 2017.

[25] H. u. Hassan, K. Govind and A. Hartmaier, "Micromechanical modelling of coupled crystal plasticity and hydrogen diffusion," *Philosophical Magazine,* vol. 99, no. 1, pp. 92-115, 2019.

[26] F. Farukh, L. Zhao, N. Barnard, M. Whittaker and G. McColvin, "Computational modelling of full interaction between crystal plasticity and oxygen diffusion at a crack tip," *Theoretical and Applied Fracture Mechanics,* vol. 96, pp. 707-719, 2018.

[27] S. Prussin, "Generation and distribution of dislocations by solute diffusion," *Journal of Applied Physics,* vol. 32, pp. 1876-1881, 1961.

[28] A. Voskamp, R. Österlund, P. Becker and O. Vingsbo, "Gradual changes in residual stress and microstructure during contact fatigue in ball bearings," *Metals Technology,* vol. 1, no. 7, 1980.

[29] R. Dommarco, K. Kozaczek, P. Bastias, G. Hahn and C. Rubin, "Residual stresses and retained austenite evolution in SAE 52100 steel under non-ideal rolling contact loading," *Wear,* vol. 257, no. 11, pp. 1081-1088, 2004.

[30] V. Güley, A. E. Tekkaya, T. Savaş and F. Özhan, "Experimental investigation of residual stresses after heat treatment and grinding processes in the production of ball bearing rings," *Materials Science Forum,* Vols. 571-572, pp. 27-32, 2008.

[31] C. A. Stickels and A. M. Janotik, "Controlling residual stresses in 52100 bearing steel by heat

treatment," *Metallurgical Transactions A,* vol. 11, no. 3, pp. 467-473, 1980.

[32] B. Gould, M. Paladugu, N. Demas, A. Greco and R. Hyde, "Figure the impact of steel microstructure and heat treatment on the formation of white etching cracks," *Tribology International,* vol. 134, pp. 232-239, 2019.

[33] A. Kumnick and H. Johnson, "Deep trapping states for hydrogen in deformed iron," *Acta Metallurgica,* vol. 28, no. 1, pp. 33-39, 1980.

[34] G. Hahn, V. Bhargava and Q. Chen, "The cyclic stress-strain properties, hysteresis loop shape, and kinematic hardening of two high-strength bearing steels," *Metallurgical Transactions A,* vol. 21A, pp. 653-665, 1990.

[35] F. Yoshida, "A constitutive model of cyclic plasticity," *International Journal of Plasticity,* vol. 16, no. 3-4, pp. 359-380, 2000.

[36] P. Sofronis, Y. Liang and N. Aravas, "Hydrogen induced shear localization of the plastic flow in metals and alloys," *European Journal of Mechanics - A/Solids,* vol. 20, no. 6, p. 2001, 857-872.

[37] R. A. Oriani, "The diffusion and trapping of hydrogen in steel," *Acta Metallurgica,* vol. 18, no. 1, pp. 147-157, 1970.

[38] J. Hirth, "Effects of hydrogen on the properties of iron and steel," *Metallurgical Transactions A,* vol. 11A, pp. 861-890, 1980.

[39] J. Toribio and V. Kharin, "A generalised model of hydrogen diffusion in metals with multiple trap types," *Philosophical Magazine,* vol. 95, no. 31, pp. 3429-3451, 2015.

[40] J. Svoboda and F. Fischer, "Modelling for hydrogen diffusion in metals with traps revisited," *Acta Materialia,* vol. 60, no. 3, pp. 1211-1220, 2012.

[41] Schaeffler Technologies AG & Co. KG, "Axial cylindrical roller bearings 81104-TV," Herzogenaurach, 2018.

[42] I. Khader, D. Kürten and A. Kailer, "A study on the wear of silicon nitride in rolling-sliding contact," *Wear,* vol. 296, no. 1-2, pp. 630-637, 2012.

[43] O. Zwirlein and H. Schlicht, "Werkstoffanstrengung bei Waelzbeanspruchung Einfluss von Reibung und Eigenspannungen," *Materialwissenschaft und Werkstofftechnik,* vol. 11, pp. 1-14, 1980.

[44] D. Systèmes, "Abaqus User Subroutines Reference Guide, Version 2018," 2018.

[45] V. Bhargava, G. T. Hahn and C. A. Rubin, "Rolling contact deformation, etching effects, and failure of high-strength bearing steel," *Metallurgical Transactions A,* vol. 21, no. 7, pp. 1921-1931, 1990.

[46] A. Warhadpande, F. Sadeghi, M. N. Kotzalas and G. Doll, "Effects of plasticity on subsurface initiated spalling in rolling contact fatigue," *International Journal of Fatigue,* vol. 36, no. 1, pp. 80-95, 2012.

[47] C. Acht, M. Dalgic, F. Frerichs, M. Hunkel, A. Irretier, T. Lübben and H. Surm, "Ermittlung der Materialdaten zur Simulation des Durchhärtens von Komponenten aus 100Cr6. Teil 1," *HTM Journal of Heat Treatment and Materials,* vol. 63, no. 5, 2008.

[48] G. Hahn, "A model for yielding with special reference to the yield-point phenomena of iron and related bcc metals," *Acta Metallugica,* vol. 10, pp. 727-738, 1962.

[49] D. Systèmes, "Abaqus Benchmarks Guide, Version 2018," 2018.

[50] D. 50125, "Pruefung metallischer Werkstoffe - Zugproben," DIN, 2009.

[51] V. Smelova, A. Schwendt, L. Wang, W. Holweger and J. Mayer, "Electron microscopy investigation of microstructural alternations due to classical Rolling Contact Fatigue (RCF) in martensitic AISI 52100 bearing steel," *International Journal of Fatigue,* no. 98, pp. 142-154, 2017.

[52] J. Franke, W. Holweger, H. Surborg, T. Blass, J. Fahl, T. Elfrath and D. Merk, "Influence of Tribolayer on Rolling Bearing Fatigue Performed on a FE8 Test Rig," in *TAE 19th International Colloquium Tribology*, Ostfildern, 2014.

[53] M.-H. Evans, L. Wang, H. Jones and R. Wood, "White etching crack (WEC) investigation by serial sectioning, focused ion beam and 3-D crack modelling," *Tribology International,* vol. 65, pp. 146-160, 2013.

[54] E. Wittek, N. Bader and G. Poll, "Tribological Properties of Fuel Economy Gearbox Oils," in *69th Annual Meeting and Exhibition, Society of Tribologists and Lubrication Engineers (STLE)*, Lake Buena Vista, Florida, 2014.

[55] S. Fujita, N. Mitamura and Y. Murakami, "Research of new factors affecting rolling contact fatigue life," in *World Tribology Congress III*, Washington, D.C., 2005.

[56] A. R. Du Crehu, Tribological analysis of White Etching Crack (WEC), vol. PhD Dissertation, Lyon: L'Institut National des Sciences Appliquées de Lyon, 2014.

[57] R. Errichello, R. Budny und R. Eckert, „Investigations of bearing failures associated with white etching areas (weas) in wind turbine gearboxes," *Tribology Transactions,* Bd. 56, Nr. 6, pp. 1069-1076, 2013.

[58] M. Oezel, A. Schwedt, T. Janitzky, R. Kelley, C. Bouchet-Marquis, L. Pullan, C. Broeckmann and J. Mayer, "Formation of white etching areas in SAE 52100 bearing steel under rolling contact fatigue – Influence of diffusible hydrogen,," *Wear,* vol. 414–415, pp. 352-365, 2018.

[59] N. Kino and K. Otani, "The influence of hydrogen on rolling contact fatigue life and its improvement," *JSAE Review,* vol. 24, no. 3, pp. 289-294, 2003.

[60] H. Uyama, H. Yamada, H. Hidaka and N. Mitamura, "The effects of hydrogen on microstructural change and surface originated flaking in rolling contact fatigue," *Tribology Online,* vol. 6, no. 2, pp. 123-132, 2011.

[61] M.-H. Evans, A. Richardson, L. Wang and R. Wood, "Effect of hydrogen on butterfly and white etching crack (WEC) formation under rolling contact fatigue (RCF)," *Wear,* vol. 306, no. 1-2, pp. 226-241, 2013.

[62] A. D. Richardson, M.-H. Evans, L. Wang, R. J. K. Wood, M. Ingram and B. Meuth, "The evolution of white etching cracks (wecs) in rolling contact fatigue-tested 100cr6 steel," *Tribology Letters,* vol. 66, 2017.

[63] J. Franke, J. T. Carey, S. Korres, T. Haque, P. W. Jacobs, J. Loos and W. Kruhoeffer, "White etching cracking - simulation in bearing rig and bench tests," *Tribology Transactions,* vol. 61, no. 3, pp. 403-413, 2018.

[64] M.-H. Evans, A. Richardson, L. Wang and R. Wood, "Serial sectioning investigation of butterfly and white etching crack (WEC) formation in wind turbine gearbox bearings," *Wear,* vol. 302, pp. 1573-1582, 2013.